NREL National Renewable Energy Laboratory

Innovation for Our Energy Future

Plasma-Assisted Co-evaporation of S and Se for Wide Band Gap Chalcopyrite Photovoltaics

Final Subcontract Report
December 2001 — April 2005

I. Repins
ITN Energy Systems, Inc.
Littleton, Colorado

C. Wolden
Colorado School of Mines
Golden, Colorado

Plasma-Assisted Co-evaporation of S and Se for Wide Band Gap Chalcopyrite Photovoltaics

Final Subcontract Report
December 2001 — April 2005

I. Repins
ITN Energy Systems, Inc.
Littleton, Colorado

C. Wolden
Colorado School of Mines
Golden, Colorado

TABLE OF CONTENTS

LIST OF FIGURES

LIST OF TABLES

1 Introduction, Goals, and Approach

In terms of small-area device efficiency and module stability $CuIn_xGa_{1-x}Se_2$ (CIGS) devices provide a benchmark for all thin film photovoltaics. Nonetheless, there is significant opportunity for improvement in manufacture of CIGS devices. First, high-quality CIGS deposition requires high substrate temperatures (>500°C), limiting the selection of substrate materials, and increasing deposition cycle times due to heat-up and cool-down periods. Furthermore, current co-evaporation technology requires overpressure of chalcogens (Se_2 or S_2) during deposition, resulting in low material utilization and high equipment maintenance costs. Furthermore, the useful available energy bandgap expansion via alloying is limited to less than 1.3eV.

In this work, ITN Energy Systems (ITN) and lower-tier subcontractor Colorado School of Mines (CSM) explore the replacement of the molecular chalcogen precursors during deposition (e.g. Se_2 or H_2Se) with more reactive chalcogen monomers or radicals (e.g. Se). Molecular species are converted to atomic species in a low-pressure inductively-coupled plasma (ICP). The thermodynamics that motivate this approach are illustrated in Figure 1. This diagram shows the changes in Gibbs free energy for $CuInSe_2$ (left) and $CuInS_2$ (right) synthesis from various chalcogen sources.[1,2] The formation energy of copper and indium are zero, so the reactant energy simply reflects the chalcogen source. Sulfur and selenium both sublime as dimers that may readily oligomerize into ring structures of S_n or Se_n, where n varies from $2 < n < 8$. However, the variation of n between 2 and 8 has relatively little effect on the reactant energy. For example, the energetics of a sublimated S source would be bound between the S_2 and S_8 values shown in the right half of Figure 1.
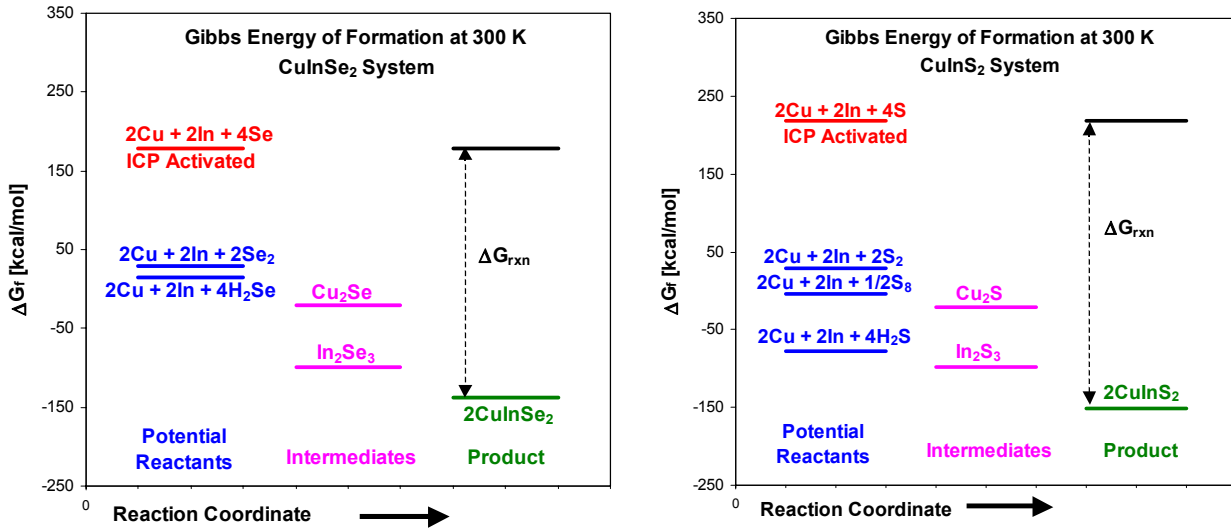
Figure 1 : Thermodynamics of $CuInSe_2$ and $CuInS_2$ formation at 300 K using various chalcogen sources.

The details of the CIS reaction pathway are still somewhat of an open question. The formation of $CuInSe_2$ may occur directly, or it may proceed through the formation of the sulfide intermediates Cu_2Se and In_2Se_3. ***In either case significant activation barrier(s) must be present since the reaction does not proceed spontaneously at ambient conditions.*** The premise of this work is to overcome these barriers by activating the chalcogen source. This premise can be illustrated by considering, for example, the energy of S in its various states. At 300 K the free energy of sublimated S is near zero. The alternative hydrogen sulfide source is significantly more stable at this temperature. Our approach is to activate these chalcogen

precursors using an inductively coupled plasma (ICP) source. In the plasma, high-energy electrons dissociate these feed gasses into atoms, excited metastables (S*), and ions (S$^+$). Atomic sulfur provides a tremendous amount of energy, as was illustrated in Figure 1. The Gibbs heat of reaction using atomic sulfur would be very exothermic, -185 kcal/mol of CuInS$_2$. Metastable and ionic sulfur would provide even more energy to the system. The selenium system behaves very similarly, but the energy differences are slightly less dramatic. The dissociation of the selenium dimer requires ~88 kcal/mol versus ~95 kcal/mol for the sulfur dimer. ICP devices have proven very efficient for dissociation of the dimers (H$_2$, O$_2$, Cl$_2$) used in chemical vapor deposition and etching processes.[3,4] The plasma kinetics of chalcogens have not been studied. However in the case of oxygen, a molecule that has nearly the same bond strength as S$_2$, nearly complete dissociation is achieved in these devices.[2]

Tasks of the proposed program centered on development and validation of monatomic chalcogen chemistry, tuning of low-pressure monomer chalcogen sources, and evaluation of plasma-assisted co-evaporation (PACE) for CIGS co-evaporation. Likely advantages of deposition by plasma-enhanced co-evaporation include:
- Provides potential for lower deposition temperature and/or for better film quality at higher deposition temperature.
- Provide potential for decreased deposition times.
- Provides high material utilization efficiency (~90%) that results in less deposition on other parts of the reactor leading to lower clean up and maintenance costs, as well as longer equipment lifetime. High material utilization efficiency also reduces the total operating pressure, which is beneficial for the design and control of metal co-evaporation. Advantages include minimal metal-vapor beam spread and lower source operating temperatures.
- Enables deposition of wide bandgap copper indium gallium sulfur-selenide (CIGSS) films with controlled stoichiometry.

University researchers at CSM have developed and tested the fundamental chemistry and engineering principles, while industrial researchers at ITN adapted PACE technology to CIGSS co-evaporation. The effect of plasma activation was first examined for binary films (In$_x$Se$_y$ and Cu$_x$Se$_y$) and gradually extended to ternary and quaternary compounds and the complete three-stage CIGS co-evaporation process. Work under this contract has proceeded in three areas: development of the plasma source hardware (section 2), examination of the film kinetics (section 3), and application of the PACE sources to CIGS fabrication by co-evaporation (section 4).

2 Plasma Source Development

2.1 *Source Hardware*

ICP sources for chalcogen delivery were operated and developed in four different configurations and over a wide range of operation conditions during this program. Three configurations used for ICP source operation are shown in Figure 2. Figure 2a shows an ICP source operating in the CSM diagnostic chamber. The diagnostic chamber is used to examine the source characteristics for low chalcogen flows, and is fitted with advanced instrumentation such as an optical emission spectrometer (OES), a quadrupole mass spectrometer (QMS), and various gauging. The ICP source, common to each configuration, is the glowing tube seen Figure 2a. The plasma is generated in a one-inch diameter quartz tube using a five turn, water- cooled copper coil powered by a 13.56 MHz RF supply and associated match network. Chalcogen vapors and Ar are fed into the tube outside the chamber. The RF plasma converts the stable vapors into highly active monomers and ions. The reactive species effuse from a small orifice at the end of the ICP device into the collision less high vacuum environment (10-5 Torr).
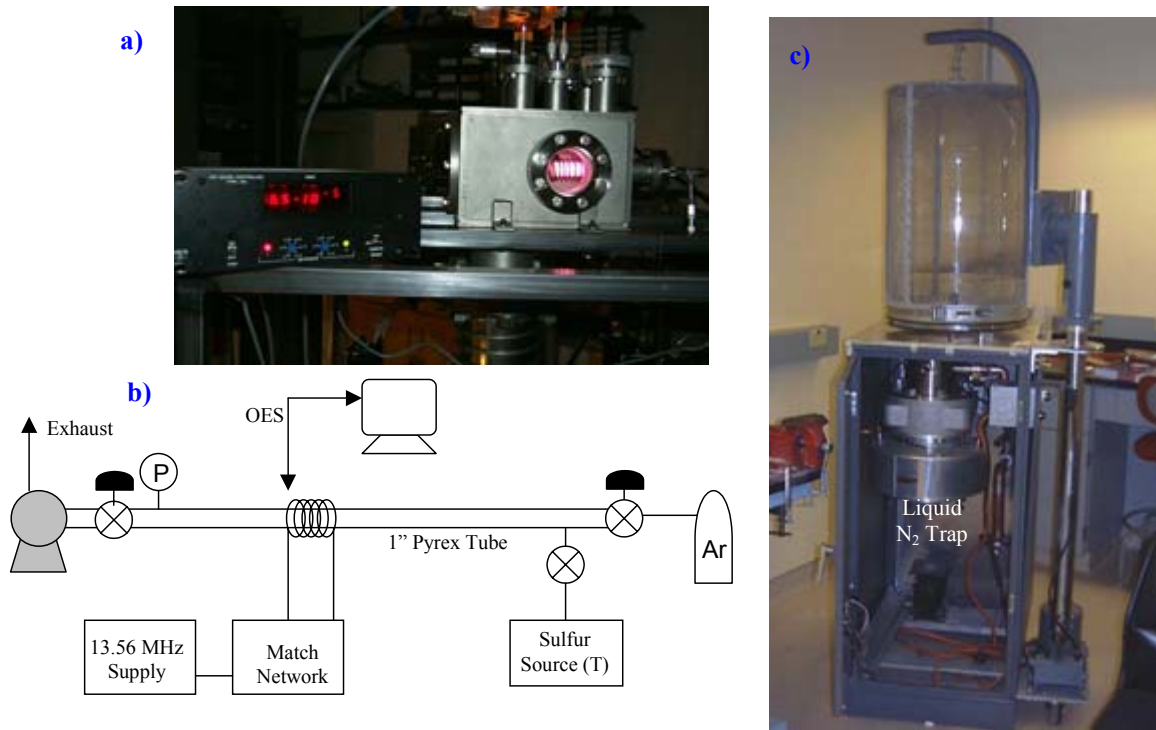
Figure 2 : ICP source in a) diagnostic chamber, b) benchtop configuration, and c) PACE chamber.

Figure 2b shows a schematic of an ICP source operating in benchtop mode. This mode is useful for tests requiring significant chalcogen flux that would contaminate the advanced instrumentation in the diagnostic chamber. The plasma is contained in a 1" diameter pyrex tube. Argon is supplied through a needle valve, while an on/off valve isolates the chalcogen effusion source. A butterfly valve on the exhaust line is used to control the pressure. The effusion source is maintained at the desired temperature through PID control. This benchtop unit is operated at the similar conditions as will be used for CIGS film depositions. The only difference is that this system is exhausted directly to a pump, instead of effusing into a high vacuum environment. The benchtop plasma source allows extensive quantification of sulfur/selenium flux and optimization ICP operation as a function of pressure, power, and composition without contamination of other equipment.

The first simultaneous exposure of a substrate to the plasma-activated chalcogens, heat, and In was performed in the PACE chamber. The PACE chamber is shown in Figure 2c. This chamber is the next step in the transition of ICP sources to full CIGSS coevaporation. It allows the study of plasma-activated binary film formation and source uniformity without the stringent requirements on temperature and multi-source flux rate monitoring imposed by CIGSS co-evaporation. The PACE chamber includes a glass bell jar with implosion shield and hoist, a cabinet for housing pumps and instrumentation, a liquid trap, diffusion pump, and pneumatic gate valve. The baseplate was modified to accommodate the ICP sources and In evaporation. Figure 3 shows a PACE source operating in the glass bell jar at CSM. On the left is shown the entire bell jar, with a close up of reactor tube shown on the right.
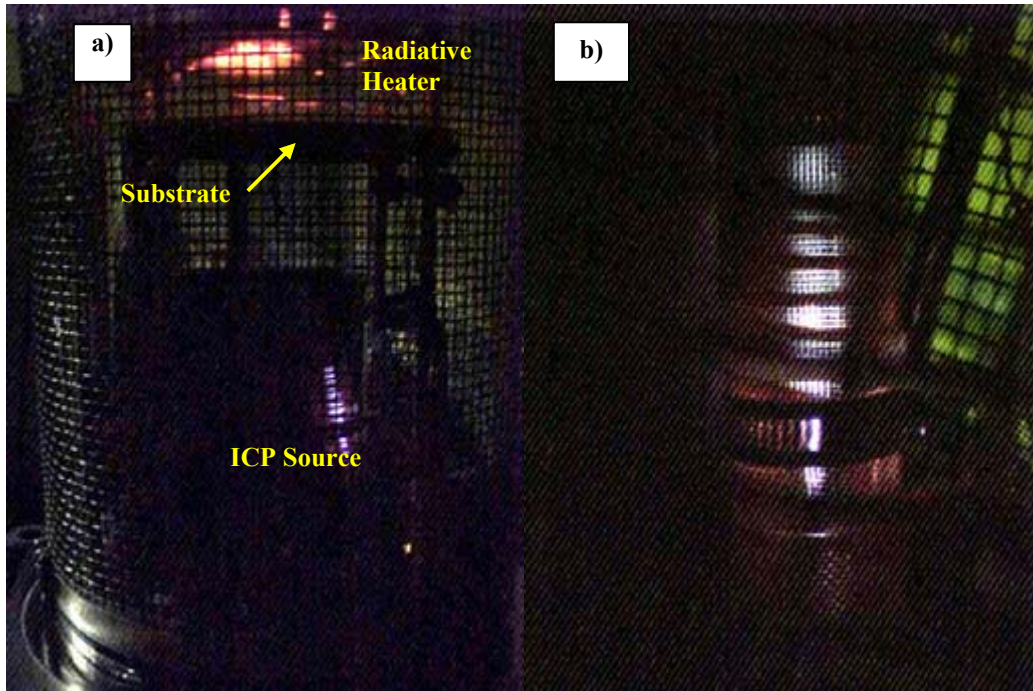
Figure 3 : PACE source operating in glass bell jar at CSM. Photos show a) entire bell jar, and b) close up of reactor tube therein.

The fourth environment used for ICP source operation was a CIGS bell jar. The bell jar design is based on that of the NREL CIGS co-evaporators, and was assembled at ITN. Co-evaporation of the elements is performed through resistive heating of small Cu, In, Ga, and Se boats, each with a capacity of several grams. Se rate is monitored by quartz crystal microbalance (QCM), and metals rates are monitored by electron impact emission spectrometry (EIES). CIGS emission, as measured by thermopile, is used for end-point detection.[5] The substrate is heated radiatively, and its temperature is monitored by thermocouple. Figure 4 shows two views of the bell jar. Figure 4a uses a cut-out view of the bell jar exterior to show the positioning of the EIES emission head relative to the deposition zone. Figure 4a utilizes a cut-out view to show the deposition zone - and the position of the EIES relative to it - with the bell jar down. The evaporation boats are located near the bottom of the cut-out. The substrate heaters and thermocouple are visible at the top of the cut-out. A copper-colored shutter is seen shielding the substrate in the top 1/3 of the cut-out. The location of the EIES emission head is level with the black photomultiplier tubes at the right of the photo. Figure 4b shows the EIES emission head affixed to the inside of the bell jar, as the bell jar descends from the open position into its deposition position on the base plate.
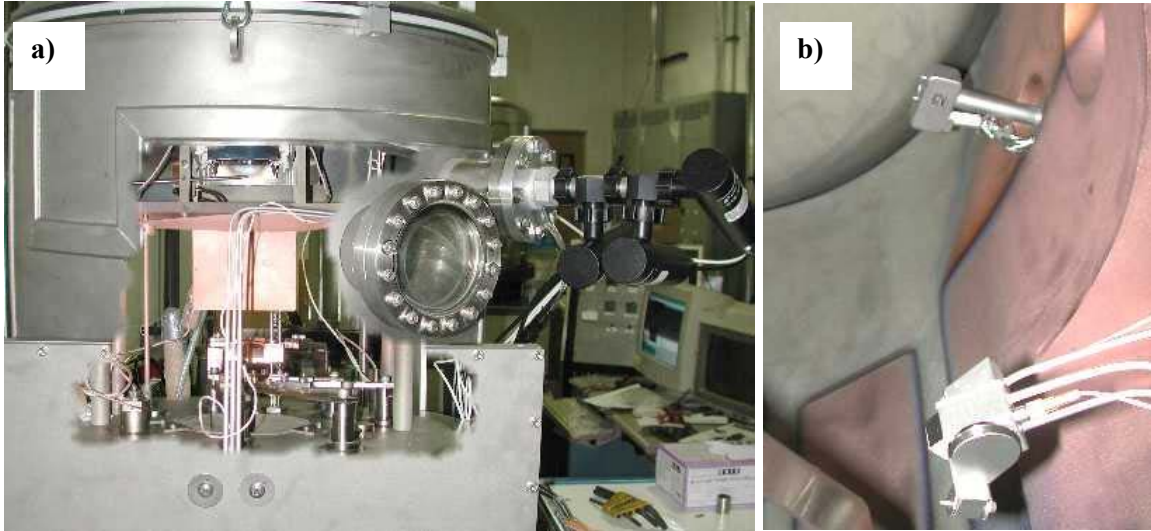
Figure 4 : Photographs of co-evaporation baseline bell jar a) with cut-out showing deposition zone and positioning of components with lid down, and b) showing EIES head position relative to bell jar wall.

2.2 ICP Source Diagnostics

An important aspect of the ICP source development is the ability to monitor deposition rate, chalcogen dissociation, and plasma characteristics such as plasma density and electron temperature. To achieve these functions, the interpretation of optical emission spectroscopy (OES) signals from the ICP sources was developed simultaneously with the sources and compared with mass spectrometry data.

The use of OES on the ICP sources was first tested on the diagnostic chamber using O_2 and N_2 gases. Figure 5 shows OES spectra from the ICP source on the diagnostic chamber for different gas flows. Figure 5a shows the spectrum with O_2 flow only, and the source operated at 60W. Figure 5b shows the spectrum with N_2 flow only, and the source operated at 40W and 60W. In the spectra of Figure 5c, both gases are flowing through the source, and the characteristic peaks of each gas are evident.
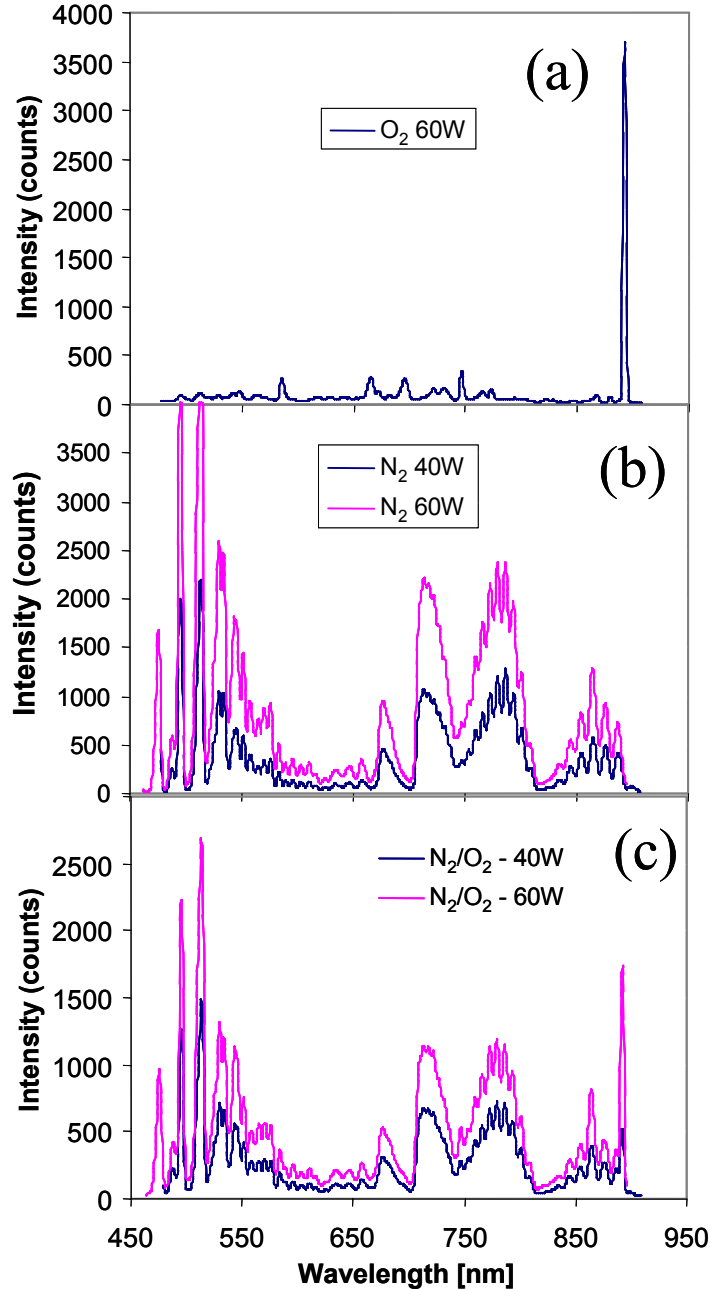
Figure 5 : OES spectra from ICP sources with flow of a) O₂, b) N₂, and c) both O₂ and N₂ gases.

The O_2 and N_2 OES spectra were then correlated with mass spectrometer data. The mass spectrometer (MS) was attached to the chamber and dual MS/ OES experiments were performed. MS signals have been cross-referenced with OES signals so that OES may be used as a real time sensor. Efforts were directed at quantifying the mass spectrometry. These included the use of laser to align the MS and the ICP unit. A beam stop was purchased, modified and installed to distinguish ICP from background signal. The mass spectrometry data demonstrate the efficacy of the ICP sources in cracking gas species such as N_2 and O_2. Figure 6 and Figure 7 show MS data demonstrating the dissociation of oxygen and nitrogen dimers. When the plasma is ignited, the parent peaks - 32 and 28 respectively - decrease while the atomic peaks (16 and 14) increase. Table 1 shows a quantitative summary of the signal changes of the previous two figures. The relatively long transients associated with the data in Figure 6 and Figure 7 is attributed to

heating of the ICP devices. This has been corroborated by simultaneous optical emission spectroscopy (OES) measurements.
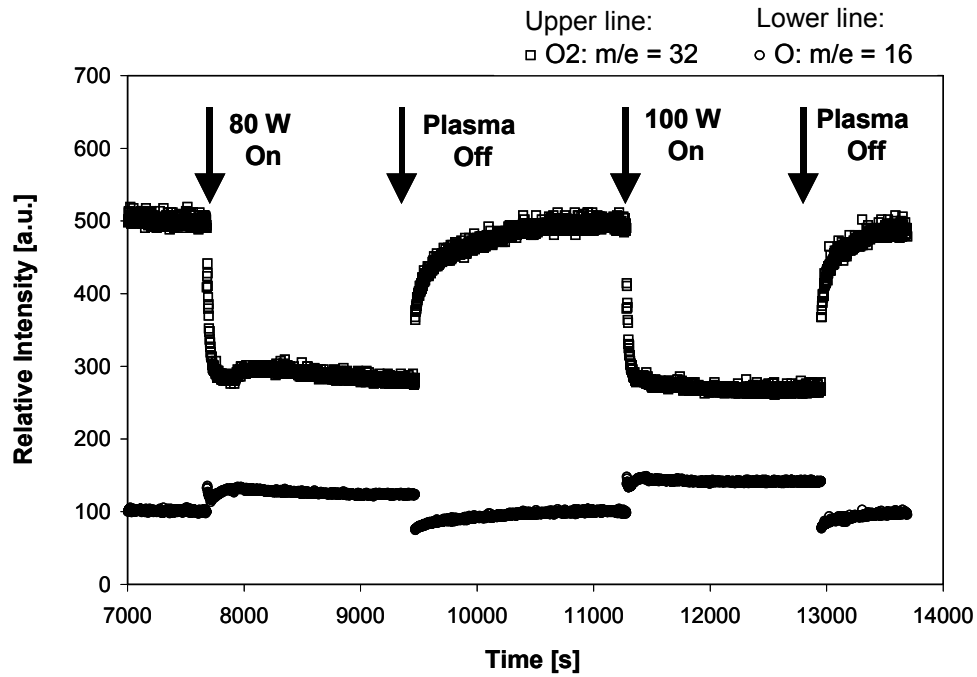
Figure 6 : MS signals for an O$_2$ Plasma.
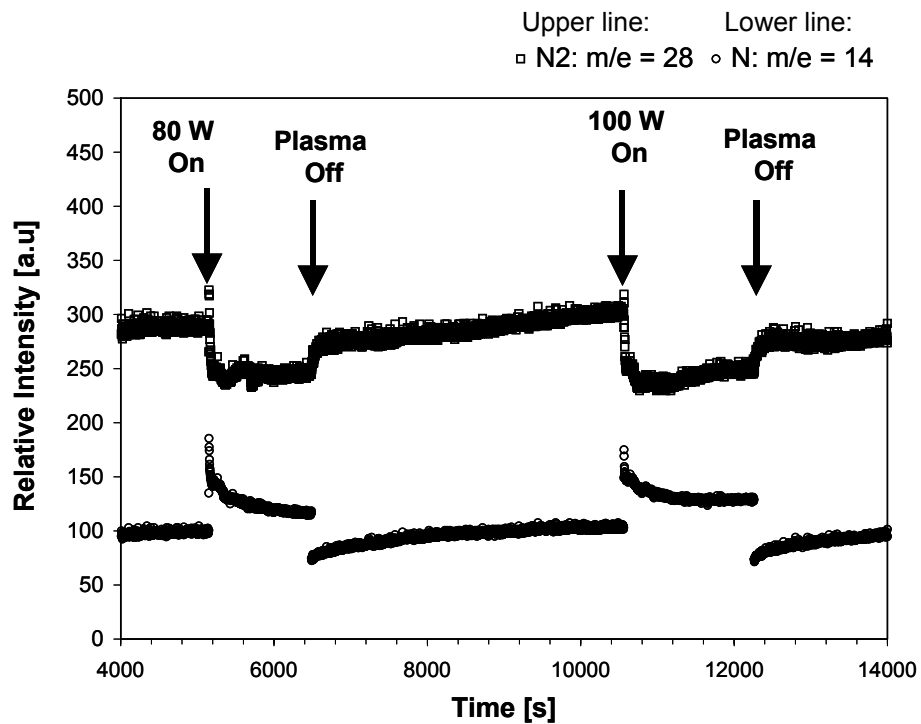
Figure 7 : MS signals for a N$_2$ Plasma.

Signal	Change for a 80 W plasma	% Change for a 100 W plasma
O_2: m/e = 32	-42%	-46%
O: m/e = 16	+25%	+42%
N_2: m/e = 28	-16.5%	-20%
N: m/e = 14	+19%	+29%

Table 1 : Summary of change in mass spectrometer signals for O2 and N2 plasmas.

Quantification of the S flux also requires some careful consideration. The S source temperature measurement is indirect. It is achieved through a thermocouple mounted outside the S source. As such, the absolute temperature of the sulfur source can vary from run to run. Similarly the absolute OES signal can vary with fiber optic placement and integration time. Actinometry was therefore developed, relying on ratio of S emission to Ar emission as the control metric for S and Se flux. Figure 8 shows plots of actinometers versus control temperature. The S lines are at 450 and 468.5 nm, while the Ar actinometer line is 737 nm.
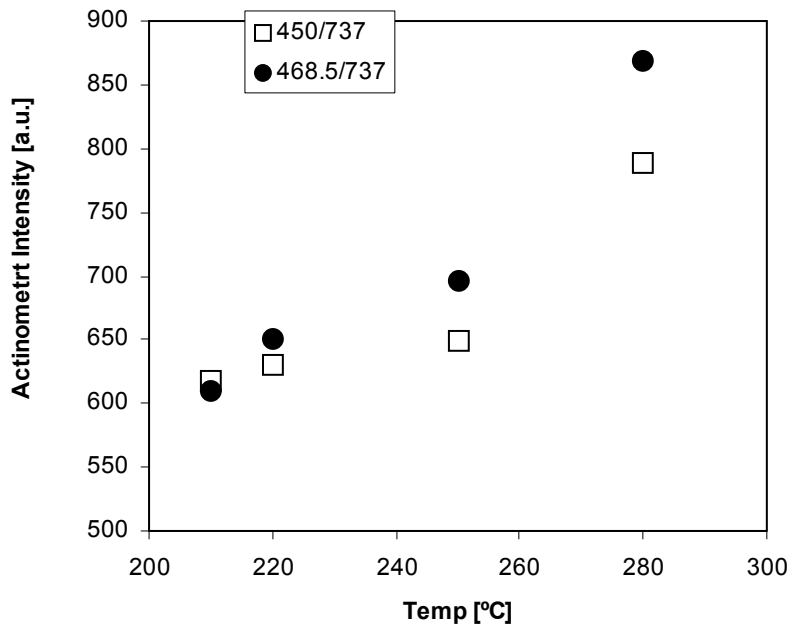
Figure 8 : Actinometers vs. control temperature for S source

2.3   ICP Source Adjustments

2.3.1   RF Leakage

A major improvement in ICP source operation in the PACE source configuration was made with the elimination of RF leakage. The leakage had adverse implications for plasma tuning and the operation of other components. A prototype Faraday cage was designed, fabricated out of copper mesh, and

implemented. The cage proved successful in eliminating RF noise to an undetectable level, an allowed tuning with near-zero reflected power. A permanent faraday cage was then constructed. In addition, improved RF connectors were obtained for both sides of the RF vacuum feedthrough. These improvements resulted in elimination of RF noise and reproducible ICP operation.

2.3.2   Pressure and Orifice Size

Satisfactory base pressures with Ar flow to the PACE source were demonstrated. Figure 9 plots the relationship between the ICP pressure as measured by a convection gauge upstream of the actual device and the PACE chamber pressure as measured by a cold cathode gauge. Since the ICP gauge is upstream of the ICP device, the true pressure in the ICP device is estimated to be ~25% of the measured pressure due to friction drop and expansion in the line. Figure 9 shows that the two pressure regimes are effectively decoupled. The chamber pressure is approximately 4 orders of magnitude less than the ICP source. Best ICP device operations occurs around 100 mtorr, which means chamber pressure will be around 10^{-5} torr for depositions. It should be noted that the relationship between ICP and chamber pressure is very sensitive to the size of the reactor tube orifice. Furthermore, the Ar pressure required for a stable plasma depends on the reactor tube geometry. Thus, as the reactor tubes are custom-made glassware, small variations from one reactor tube to the next may cause a significant modification to the relationship graphed in Figure 9.
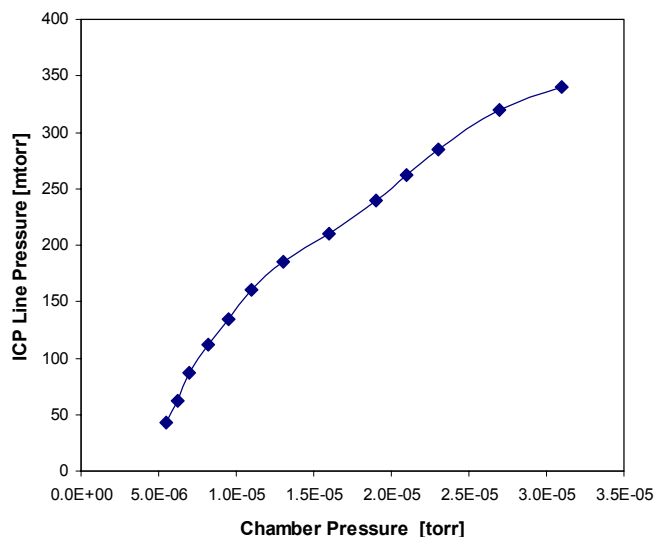
Figure 9 : Relationship between ICP line pressure and PACE chamber pressure.

2.3.3   Chalcogen Delivery

During initial tests, ICP sources were operated in the benchtop configuration to examine methods of supplying S and Se to the plasma reactor tube.

Figure 10 shows photographs of the source in operation with both an Ar plasma and an Ar/S plasma. A heated sparger filled with S shot was used to supply S vapor to the plasma. Stable sulfur/argon plasmas were obtained over a range of powers (30 – 100 W) with minimal reflected power (< 3 W), and the plasmas were stable over a large pressure range (20 – 200 mTorr). For most conditions the Pyrex wall remained clear (no S condenstion) throughout the majority of experiments. The exception was extremely high sulfur effusion temperatures.
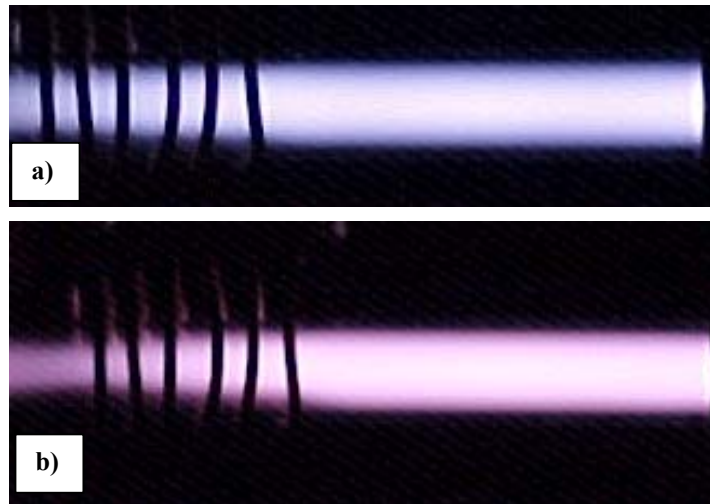
Figure 10 : ICP source in operation with both a) Ar plasma, and b) Ar/S plasma.

A fiber optic-based optical emission spectroscopy (OES) system was then used to characterize the plasmas and relate chalcogen rates to OES signal, allowing use of OES as a rate monitor. Representative OES spectra are shown in Figure 11. The S-containing plasma clearly shows the bands from 290-540 nm associated with the $B^3\Sigma^-$ transitions of electronically excited sulfur. The pyrex tube absorbs signal for wavelengths less than 350 nm.
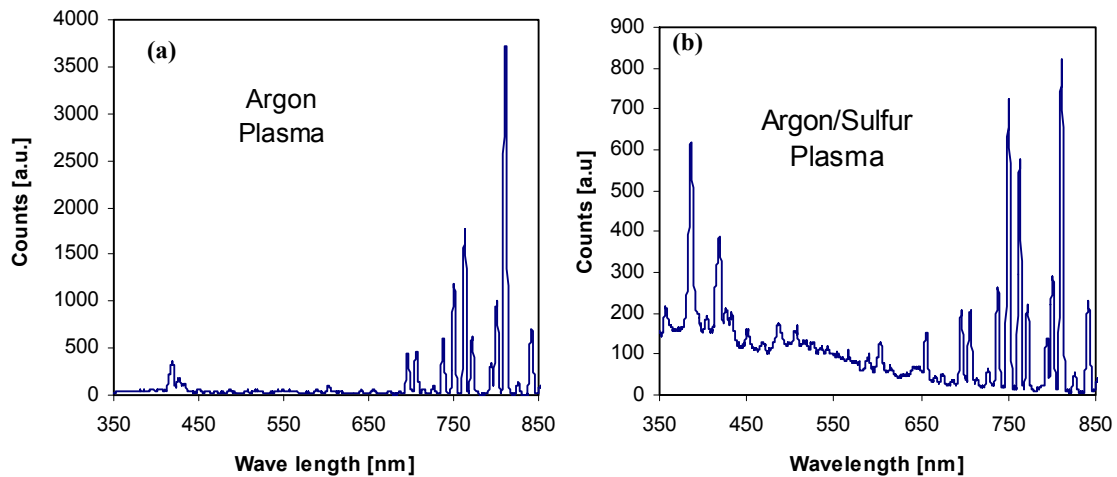
Figure 11 : OES spectra of a) an Ar plasma and b) and Ar/S plasma.

Similar data were taken for the examination of Se delivery from the ICP source. A source similar to the S source was fabricated for Se vaporization and the first Ar/Se plasma spectra was obtained. Figure 12 shows a representative spectrum. The main peaks of interest are in the region around 325-355 nm and a distinct peak at 376 nm. It is important to note that these peaks are out of the range of the S spectra, whose main peaks are located $400 < \lambda < 600$ nm. Thus, if both S and Se were activated in the same ICP source, the contributions of each chalcogen to the OES spectra could be deconvolved.
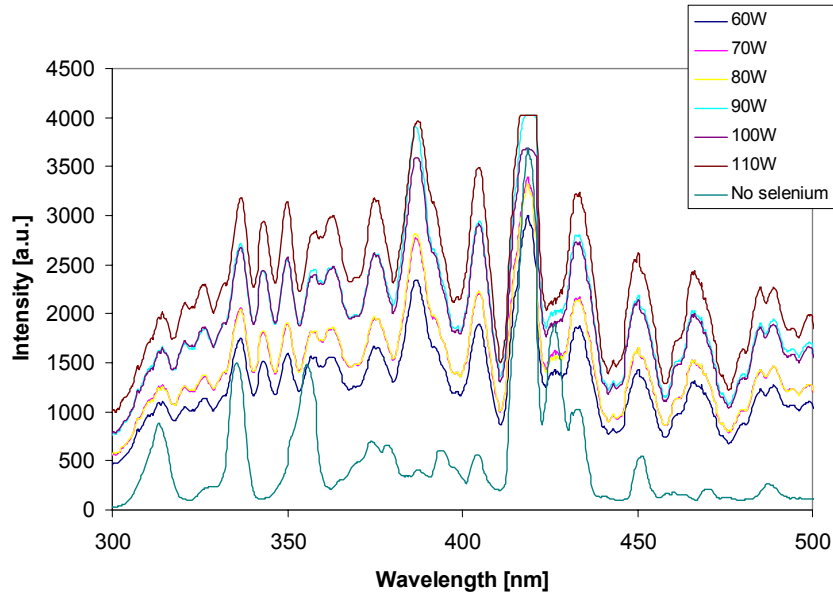
Figure 12 : Se spectra versus power.

The sparger method of chalcogen delivery poses several difficulties. First, since the gas temperature is always less than the source temperature ($T_g < T_s$), it is inherently susceptible to nucleation and condensation. Second, due to the thermal mass of the effusion source and the heating arrangements the time constants are large, causing frequent overshoot of the desired rate set point.

One possible solution is to reverse the heated elements, utilizing a cold chalcogen source and a hot carrier gas. Two advantages result. First, the gas temperature is always greater than the source ($T_g > T_s$), eliminating the possibility of gas-phase nucleation and condensation. Second, the time constants are much shorter. Gas heating was achieved using immersion heaters that work by transporting the gas across resistively heated wires. The rapid response of both the heating elements and the low thermal mass of the gas allow for rapid turn on, turn off, and enable real time control. The source tubes were prepared by loading a known amount of chalcogen in a tube, purging it with argon, and sealing it. It was then put into a furnace where it will be slowly heated and cooled, vaporizing the chalcogen and allowing it to recondense as a uniform film on the inside of the tube. This is analogous to the preparation of source plates used for CdTe deposition or $CdCl_2$ treatment in close space sublimation. These approaches are illustrated in Figure 13. In the first approach, chalcogen flux is controlled mainly by the effusion source temperature. Advantages of this first approach include large source capacity and capabilities for high Se pressures. In the second approach, chalcogen flux is controlled mainly by the hot carrier gas temperature.
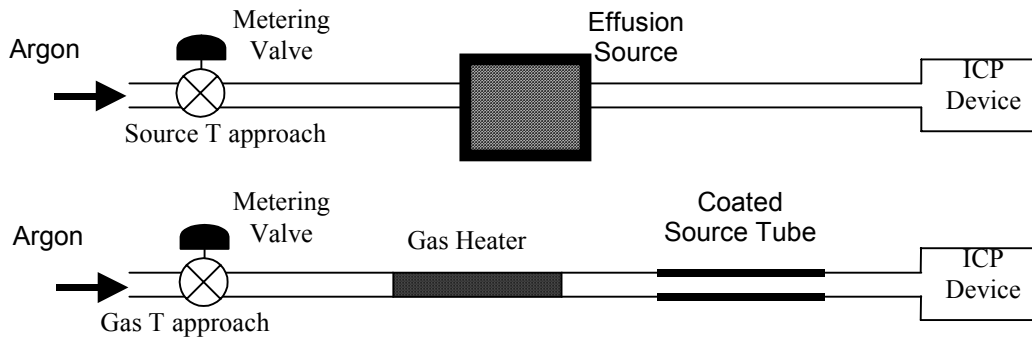
Figure 13 : Schematic comparison of two approaches for chalcogen delivery.

For implementation into CIGS co-evaporation, a hybrid of the two approaches described was used. Ar was heated prior to introduction into the source, to prevent condensation. A sparger, instead of coated plates, was used to allow adequate capacity for a full deposition. A tightly-sealed stainless steel source utilizing high voltage and low current heating rods was fabricated. Use of molecular beam epitaxy and valved thermal cracker sources was also investigated but not pursued due to high cost. Acceptable rate control was achieved by minimizing sparger thermal mass, avoiding Se condensation via heating vapor tubing and the Ar gas prior to its entry to the source, and tuning proportional integral derivative (PID) control loops. Figure 14 shows Se rate as a function of time for the source, both with and without the quartz plasma tube in place. Rate was measured by a QCM placed 1" above the source opening. Se rate control is not as tight as that achieved using the coated-plate sources in the benchtop system, but is still inside an acceptable envelope for CIGS co-evaporation, with the added benefit of adequate capacity. Source temperatures at the Se melt and at the source nozzle are also shown in Figure 14.
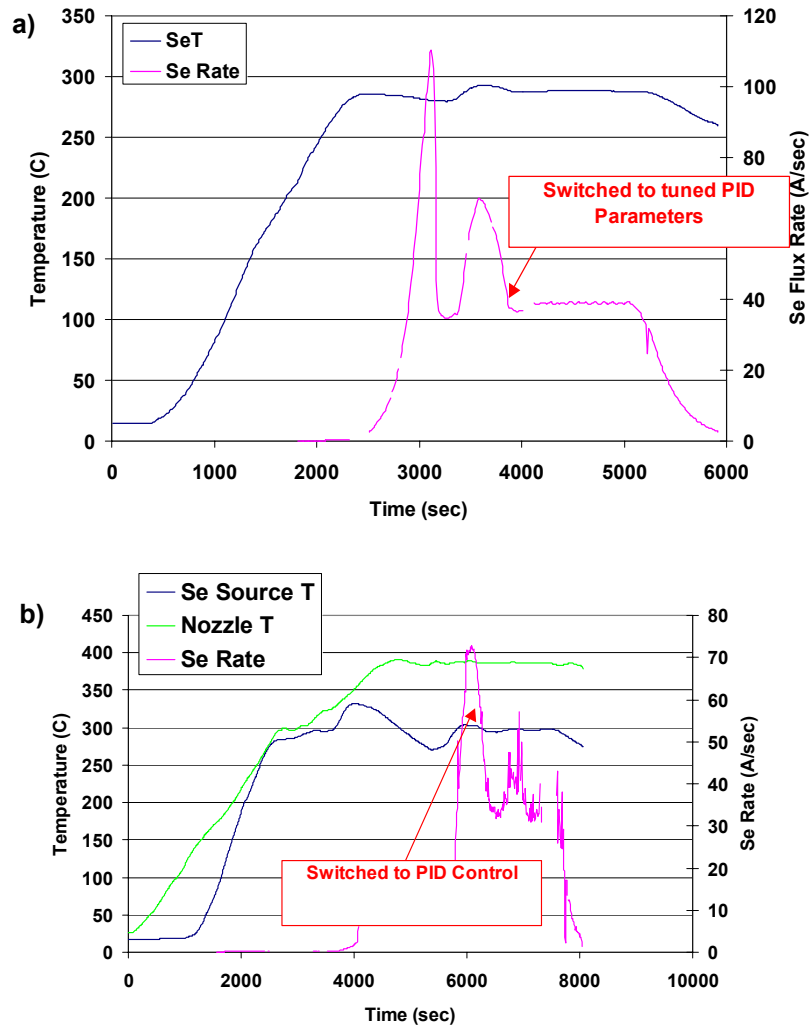
Figure 14 : Se rate from PACE effusion source a) without and b) with quartz reactor tube. Effusion source temperature is also shown.

Additional experiments were attempted in the benchtop source at high Se rates, commensurate with those required during industrial three-stage CIGS deposition. However the flux was difficult to control, and the ICP tube became coated with Se. Under these conditions, a plasma cannot be maintained.

For more precise control of the plasma and the chalcogen flux at high rates, plumbing was installed to the benchtop source for utilization of H_2S. This H_2S equipment is capable of delivering H_2S/Ar mixtures with precise control over arrange of H_2S concentrations ranging from 0.5–10% using calibrated metering valves. Preliminary experiments indicated that the plasma is highly capable of full dissociating H_2S. Using a 1% mixture, the quartz tube downstream of the ICP coil was coated with yellow solid sulfur after just minutes of operation. It was also observed that there was significant substrate heating when H_2S is introduced into the plasma. This is attributed to the exothermic recombination of atomic hydrogen on the susceptor.

The use of H_2S raises safety concerns, which were addressed using the following safety measures:
- The cylinder containing the 10% H_2S/Ar mixture is mounted in a ventilated fume hood.
- An emergency shut off valve was installed, which is position in a ventilated box.
- Two portable H_2S monitors with ppm sensitivity are mounted on the apparatus
- The entire setup was rigorously leak tested.
- A standard operating procedure (SOP) was established to ensure that all lines are completely vented of H_2S both before and after operation.
- The Experimental setup and SOP were reviewed and approved by the CSM Environmental Health and Safety (EHS) office.

The CSM EHS would not approve the utilization of the more toxic Se-containing gas, H_2Se, in any configuration.

Stable plasma operation was demonstrated over many hours. There was no evidence of sulfur condensation on either the inside or outside of the ICP device. This lack of coating is in sharp contrast to previous experiments with elemental S vapor, where S condensation was always a concern. One reason for the difference may be heating associated with atomic hydrogen recombination. It was observed that the substrate was heated to temperatures ~ 250 ºC when H_2S was added to argon plasma. Such a degree of heating would be sufficient to ensure that the sulfur is completely volatile.

Actinometry was employed to study the changes in the relative density excited sulfur species as a function of composition. All signals were normalized by the emission intensity and density of the argon line at $\lambda = 706$ nm. Figure 15 plots the relative density as a function of the %H_2S in the ICP device. All of the signals increase monotonically with %H_2S, and all display the same functionality. This is shown by the plot of [S]/sum of all S-containing species. It remains essentially constant. This indicates that the ditribtuion of species (S vs. S_2 vs. S_3, etc.) stays essentially constant with % H_2S in Ar. The highest fraction of H_2S that has been successful operated in the plasma is studied was 5 %.
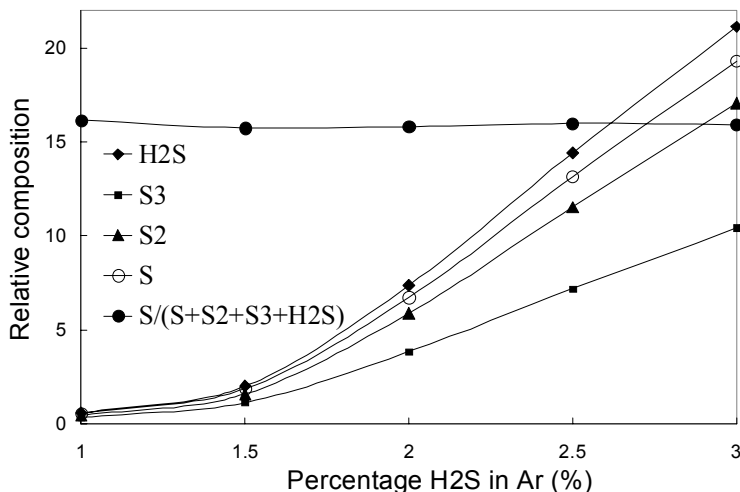
Figure 15 : Changes in relative density of sulfur-containing species as a function of initial H_2S content.

2.3.4   Uniformity

An understanding of the flux profile from the PACE sources is very important to determine acceptable geometries for installation of the PACE sources in the CIGS three-stage bell jar. A thorough characterization of the flux profile from the PACE source indicates that flux follows the expected $1/r^2$ fall-off with distance from the source, as well as the expected[6] $\cos^3\theta$ dependence of flux per solid angle on azimuthal angle, independent of Se rate and Ar pressure.

Experiments leading to this conclusion were performed at a variety of Se rates and Ar pressures, with witness slides placed around the source in the configuration of Figure 16. Se thickness at several points on each witness slide was measured by mechanical profilometer. In Figure 16, z is the vertical distance from the source aperture to the plane of a given witness slide. R is the distance from the aperture to any measurement point, and θ is the angle between $\vec{R}$ and the source axis. If flux per solid follows a $\cos^n\theta$ dependence and is constant with increasing R (i.e. neither Se-Se nor Se-Ar collisions cause significant spreading of the flux after it leaves the aperture), then it can be derived that

$$\frac{Flux\ at\ measurement\ point\ (z,R)}{Flux\ on\ axis\ at\ distance\ z_0} = \left(\frac{z}{R}\right)^{3+n}\left(\frac{z_0}{z}\right)^2$$

(1)

This expression includes the necessary factors for dependence of flux on θ, distance to slide, and angle between slide and direction of flux. A similar expression can be derived for a source axis that is not normal to the substrate plane.
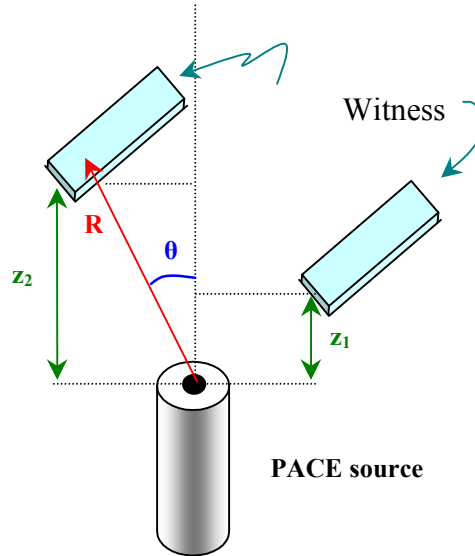
Figure 16 : Configuration for measuring flux distribution of PACE source.

Experimental verification of the expected flux profile (1) for multiple source operating conditions is shown in Figure 17. In Figure 17a, discrete points show thickness measured on multiple witness slides (as per Figure 16) graphed against R. Lines show a least squares fit to the flux profile, with n as the adjustable parameter. Figure 17b lists the test conditions and best fit n for each deposition. The distribution is invariant over the range explored: 3x variations in Ar pressure, 2x variations in rate, and 2x variations in distance. The data of Figure 17 enable prediction of flux to the substrate and its uniformity for any geometric configuration of the PACE source into the three-stage CIGS bell jar.

a)

Normalized Thickness (Arbitrary units) vs Nozzle to Measurement Point Distance (in.)

b)

Deposition #	Line Ar Pressure (mTorr)	z (in)	On-axis rate at z (Å/sec)	n from fit
217	280	4	40	3.3
218	480	4	40	3.4
219	280	4	80	3.4
213	150	8	40	3.8
213	150	6	NA	3.8
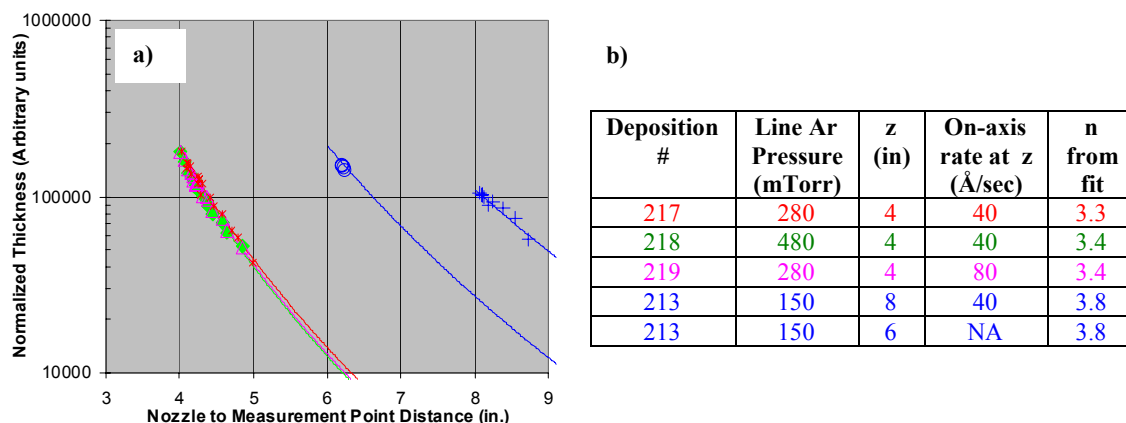
Figure 17 : Measurements of PACE source flux profile under different operating conditions.

2.3.5 Source Length

Improvements were also made to the PACE source length. The first source designed, shown on the left side of Figure 18, was more than 14" in length. This original dimension makes incorporation into CIGS co-evaporation impractical: It is longer than the distance from the baseplate to the substrate in ITN's bell jar. Several steps were taken to decrease source length. First, a gooseneck was built into the source interconnects. However, decreased rate controllability, most likely due to limited flow of Se vapor through the gooseneck, was observed. Next, all unnecessary length was trimmed from each component. The resulting design, shown on the right side of Figure 18, is approximately 5.5" tall. In Figure 18, most of each reactor tube is covered by metal shielding. Thus, the inset shows a magnification of the reactor tube orifice to indicate where Se exits the source.

3 Plasma-Assisted Film Kinetics

The film kinetics essential to the use of plasma-assisted processing were examined via two techniques. In the first technique, metallic precursors were introduced into the benchtop source (Figure 2b) and their reaction was studied as a function of source operating conditions, such as power, chalcogen rate, sample temperature, etc. In the second technique, the PACE chamber (Figure 2c) was used to co-expose a substrate to the chalcogen and one metals flux, and the resulting films were characterized as a function of operating conditions. Results and conclusions from the benchtop source technique are given below in section 3.1, while those from the PACE chamber are given in section 3.2.

3.1 Selenization and Sulphurization of Precursor Films

Experiments examining film kinetics via exposure of metallic precursors to the benchtop source (Figure 2a) are described below. The major findings are the following:
- Films treated at the highest temperature thermally showed no or little chalcogen conversion.
- The binary b-In_2S_3 phase was formed at 250 ºC, while ternary and quaternary phases were formed by plasma processing at 350 ºC in less than one hour.
- Films with well-defined XRD patterns were also characterized by proper optical band gaps and a well-defined polycrystalline morphology.

Three material systems (In, Cu-In, Cu-In-Ga) were successfully converted to sulfides and selenides using plasma processing.
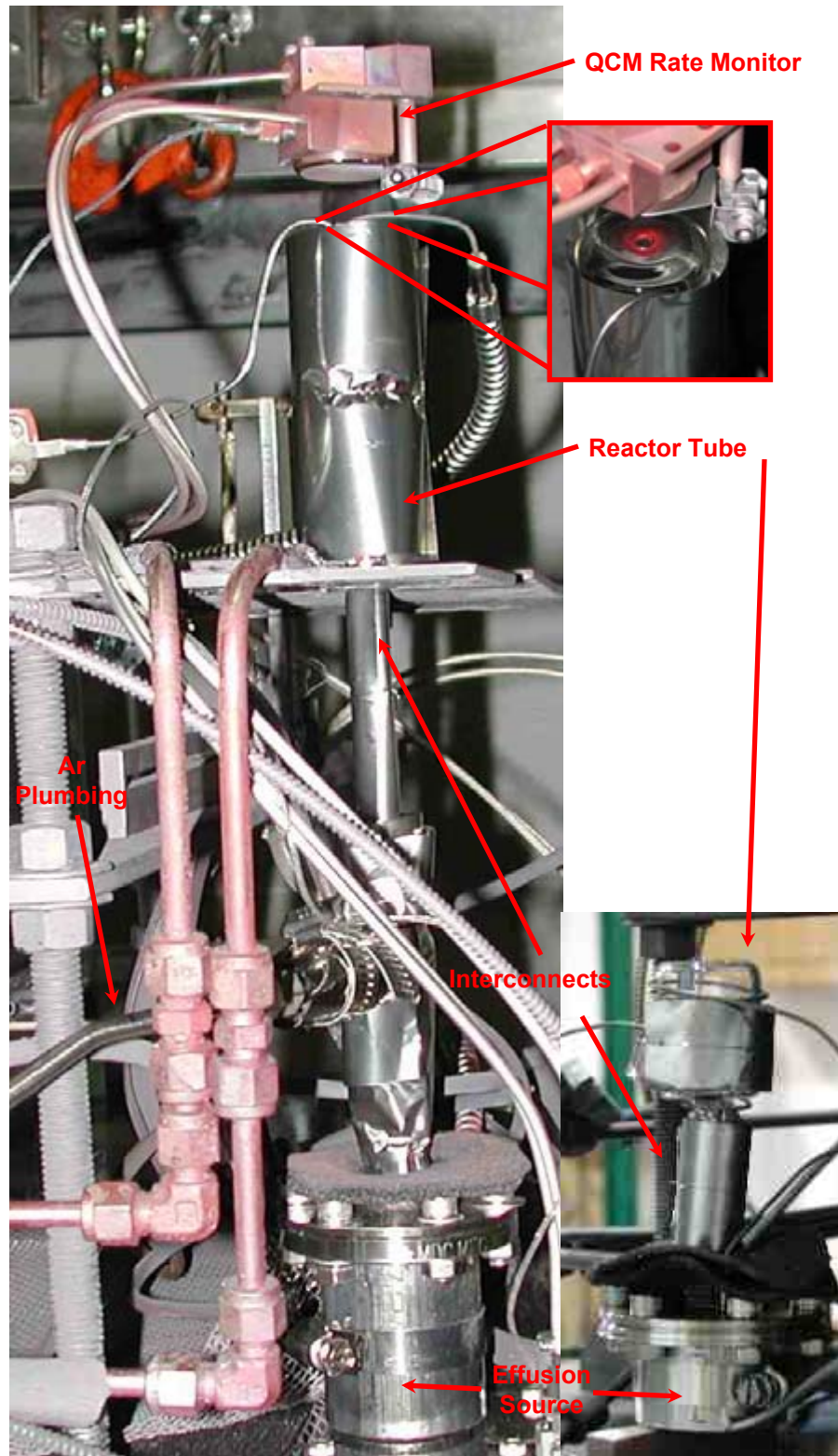
Figure 18 : Photos of first (left) and more compact (right) source designs shown 50% of actual size. Inset is magnification of reactor tube orifice.

3.1.1 β-In₂S₃ Formation

Indium films of ~ 300 nm thickness were deposited on glass substrates by thermal evaporation. These samples were exposed to a mixture of 1.5% H_2S in argon as a function of substrate temperature, with and without plasma treatment. For all experiments described here, the plasma source was operated at a total pressure = 70 mTorr, RF power = 100W, and an exposure time of 35 minutes. It was found that exposure to an argon plasma results in a substrate temperature rise of ~100-110 ºC without external heating due to ion bombardment. Exposure to the H_2S/Ar plasma mixture resulted in significantly more heating, with a minimum substrate temperature ~210 ºC for RF power 100W. This difference was attributed to surface recombination of atomic hydrogen,[7] an exothermic process which shows that H_2S was effectively dissociated under these conditions. Sulfur condensation was also observed on the quartz tube downstream of the plasma coil, which is additional evidence that the plasma effectively dissociates H_2S into sulfur and atomic hydrogen. Indium films were exposed to H_2S at substrate temperatures from 210-350 ºC, with and without plasma activation. The PID- controlled heater was employed for experiments performed without plasma, or those using temperatures greater then 210 ºC.

Films were analyzed by XRD and spectrophotometry. Figure 19 shows the resulting XRD patterns. The as-deposited film was polycrystalline indium with preferential orientation in the (100) direction. For the film treated thermally at the maximum temperature of 350 ºC, little conversion occurred. The indium diffraction peak remains strong, and only a weak In_6S_7 peak is observed. In contrast, all the films exposed to plasma formed new diffraction peaks that were positively identified as β-In₂S₃. At T_s = 210 the film was partially converted, as both In and In_2S_3 peaks are present. Plasma-treated films at temperatures ≥ 250°C contain only β-In₂S₃ peaks. The optical characterization confirms the XRD results. Wavelength dependent absorption coefficients (α) were extracted from transmission spectra and film thickness. Figure 20 shows plots of $(\alpha\varepsilon)^2$ vs. ε, where ε is the photon energy. The optical band gap is determined by extrapolating the linear portion of the curves to the x-intercept.[8] The films at T_s ≥ 250°C show a band gap of ~ 2.5 eV, which is in good agreement with literature values for β-In₂S₃.[9] The film at T_s ~210°C exhibits a lower value of 2.15 eV, consistent with the partial conversion observed by XRD. All thermally treated samples remained opaque. Results show that β-In₂S₃ may be readily formed with plasma activation of H_2S at temperatures of 250°C.

Figure 19: XRD patterns of indium films exposed to the 1.5% H_2S as a function of substrate temperature, with and without plasma activation.
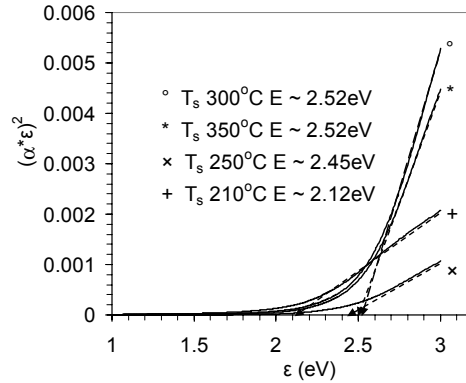
Figure 20:   Plots of (αε)² vs. ε of plasma–treated indium films at different temperatures. Band gaps were estimated by the intercept of the linear portion of the curves with the x axis.

3.1.2   CuInS₂ Formation

Co-evaporated Cu/In films deposited were exposed to H_2S plasma for 40 minutes as a function of temperature. The plasma conditions were the same as the indium sulphurisation experiments described above. Two sets of Cu/In films were used. The first set were deposited on molybdenum-coated stainless steel and were copper poor, with a Cu/In atomic ratio of 0.8 and a total thickness of 730 nm prior to sulphurisation. The second set of films were stoichiometric with Cu/In ratio of unity and were deposited on glass. Films were plasma treated at substrate temperatures of 230 -350 ºC, with and without plasma activation.

Figure 21 shows the resulting XRD patterns. Again, films treated thermally up to the maximum temperature of 350 ºC showed no evidence of conversion. In contrast, chalcogen conversion was observed in the case of all plasma treated films. The copper-poor samples exposed to plasma all resulted in a mixture of binary and ternary phases at all temperatures. The presence of the binary indium sulfide phases was attributed to the stoichiometry of the precursor films. The copper is fully consumed in the chalcopyrite phase, while excess indium is left in binary phases. In the case of stoichiometric sample only the ternary $CuInS_2$ was observed at T_s =350 ºC.   The optical band gap of this film was 1.5 eV, as expected for the ternary semiconductor.
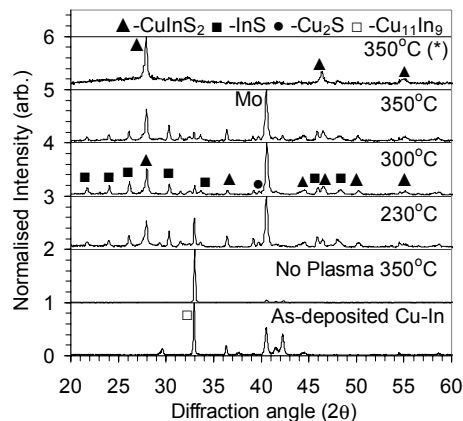
Figure 21:   XRD patterns of Cu/In films exposed to 1.5% H_2S as a function of substrate temperature, with and without plasma activation. All films shown employed Cu poor precursors (Cu/In =0.8), with exception (*) of the top pattern which was stoichiometric.

18

3.1.3 $CuIn_xGa_{1-x}S_2$ Formation

The third material system examined used sputtered Cu/In/Ga films deposited on molybdenum-coated stainless steel. The precursors were again copper poor with a Cu/(In+Ga) ratio of 0.83. The gallium fraction Ga/(In+Ga) was 0.28, and the total thickness was 648 nm prior to sulphurisation. A small amount of unintentional selenium, resulting in a Se fraction Se/(Cu+In+Ga) of 0.016 was also present in the films, due to contamination during sputtering. These films were treated at temperatures of 230 - 350 ºC, with and without plasma activation.

Figure 22 shows the resulting XRD patterns. There is almost no change in the XRD pattern of the film treated thermally at 350 ºC. The plasma treated films all showed formation of the ternary and/or quaternary chalcopyrite (i.e. $CuInS_2$ or $CuIn_xGa_{1-x}S_2$) phases. The film exposed at 230ºC was only partially converted, as there is a significant amount of polycrystalline indium remaining in the film. For temperatures at 300 and 350ºC, the films appeared to be fully converted to chalcopyrite phases. The films appear to be primarily a mixture of ternary CIS/CGS phases. The (112) peak at $2\theta \sim 26.7º$ is very broad indicating the presence of both phases instead of a single quaternary.   The 300 ºC sample was also subjected to 400ºC temperature for 2 minutes at the end of the experiment due to heater malfunction. This explains why the XRD pattern of the 300ºC film was somewhat superior to that from the 350 ºC sample. Interestingly, there is very little evidence of binary phases as was observed with the Cu/In samples (Fig. 6). There are a couple of possible reasons. These Cu-In-Gas films were sputtered, and perhaps are more reactive than the co-evaporated Cu-In films. Another possibility is that the small amount of unintentional selenium present in the films enhanced the reactivity. The window of Cu/In compositions that can be converted to the ternary chalcopyrite formation appears to be larger in the case of selenium. Films with Cu/In ratios as low as 0.8 routinely form ternary $CuInSe_2$, without the presence of binary phases. As shown above, in the case of the sulfur both ternary and binary phases are present.   The presence of the unintentional selenium may explain the absence of the binary phases for the Cu-In-Ga samples.
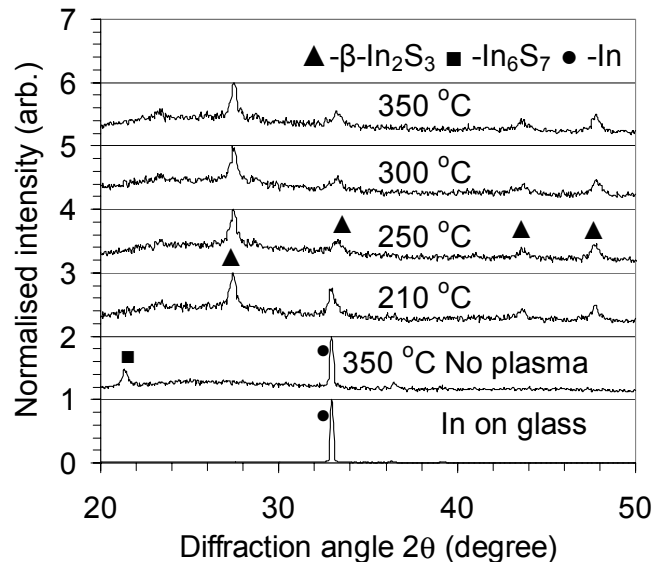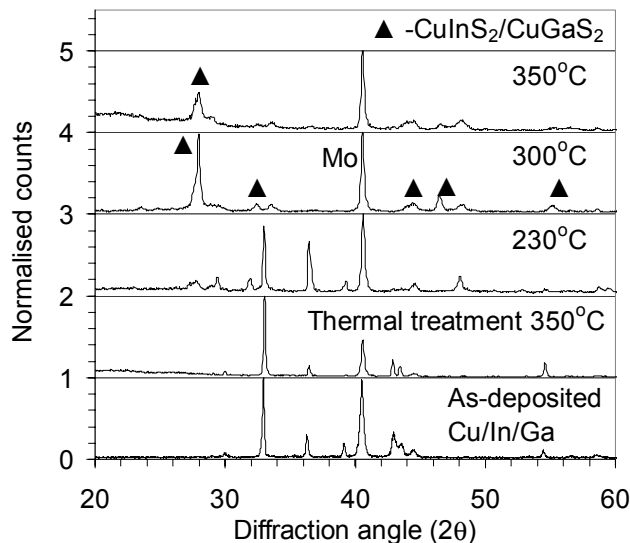

Figure 22: XRD patterns of Cu/In/Ga films exposed to the 1.5% H_2S as a function of substrate temperature, with and without plasma activation.

The copper-poor Cu/In samples on molybdenum were also exposed to selenium vapor plasma. Figure 23 shows the results from an experiment with a substrate temperature $T_s = 320ºC$, 80 W, a selenium source temperature of $T_{se} = 232$ ºC, and a process time of 55 minutes. The Figure 23 also shows the XRD pattern of thermal selenization at 350 ºC without plasma activation performed with a higher selenium flux using $T_{se} = 248$ ºC. With plasma activation the film was converted into the ternary chalcopyrite, and no crystalline binary phases (i.e. In$_2$Se$_3$, CuSe) were observed. The primary peaks observed for CuInSe$_2$ were (112), (200), (204/220) and (116/312) with strong 112 orientation. This was somewhat interesting as copper–poor alloys such as these typically prefer the (204/220) orientation in conventional thermal selenization experiments.[10] In the case of sample without plasma activation little evidence of ternary chalcopyrite phase formation was observed.
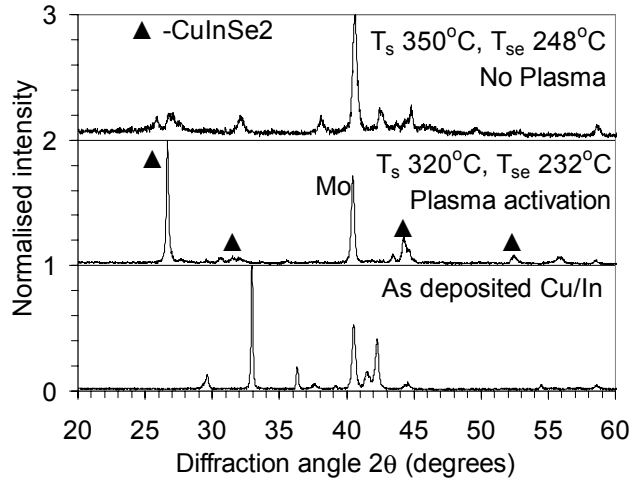
Figure 23: XRD patterns of Cu/In films exposed to the selenium with plasma activation at 320ºC and without plasma activation at 350ºC.

Up to this point we have used XRD as the primary metric of evidence for sulphurisation /selenization. As shown earlier, XRD correlated well with the optical bandgap in the case of β-In$_2$S$_3$ and CuInS$_2$. Here we show that XRD also correlates well with surface structure and morphology. Figure 24 compares the XRD patterns and morphology from three Cu/In/Ga films subjected to different degrees of selenization at substrate temperature 350 ºC. The first film was thermally selenized at high selenium flux (T_{se} ~248ºC). The resulting XRD pattern (A) shows only minimal conversion. The corresponding micrograph shows a filamentary morphology, consistent with presence of condensed selenium. The second film (B) has an XRD pattern that includes both distinct CuInSe$_2$ and CuGaSe$_2$ phases in the XRD pattern. This film was exposed to plasma, but with a low selenium flux (T_{se} ~205ºC). The corresponding SEM shows a cauliflower-like or nanocrystalline morphology. Finally, the third sample (C) is from a film that exhibits the quaternary CuIn$_x$Ga$_{1-x}$Se$_2$ phase. This sample was exposed to plasma with a higher flux of selenium ($T_{se} = 232$ ºC). The quaternary phase was readily identified by the peak shifts that occur due to the changing lattice constants.[11] The (112) peak position is centered at 26.9º, as opposed to 26.65º in the case of CuInSe$_2$. The film has distinct polycrystalline morphology with uniform grains of about ~1 μm in size.
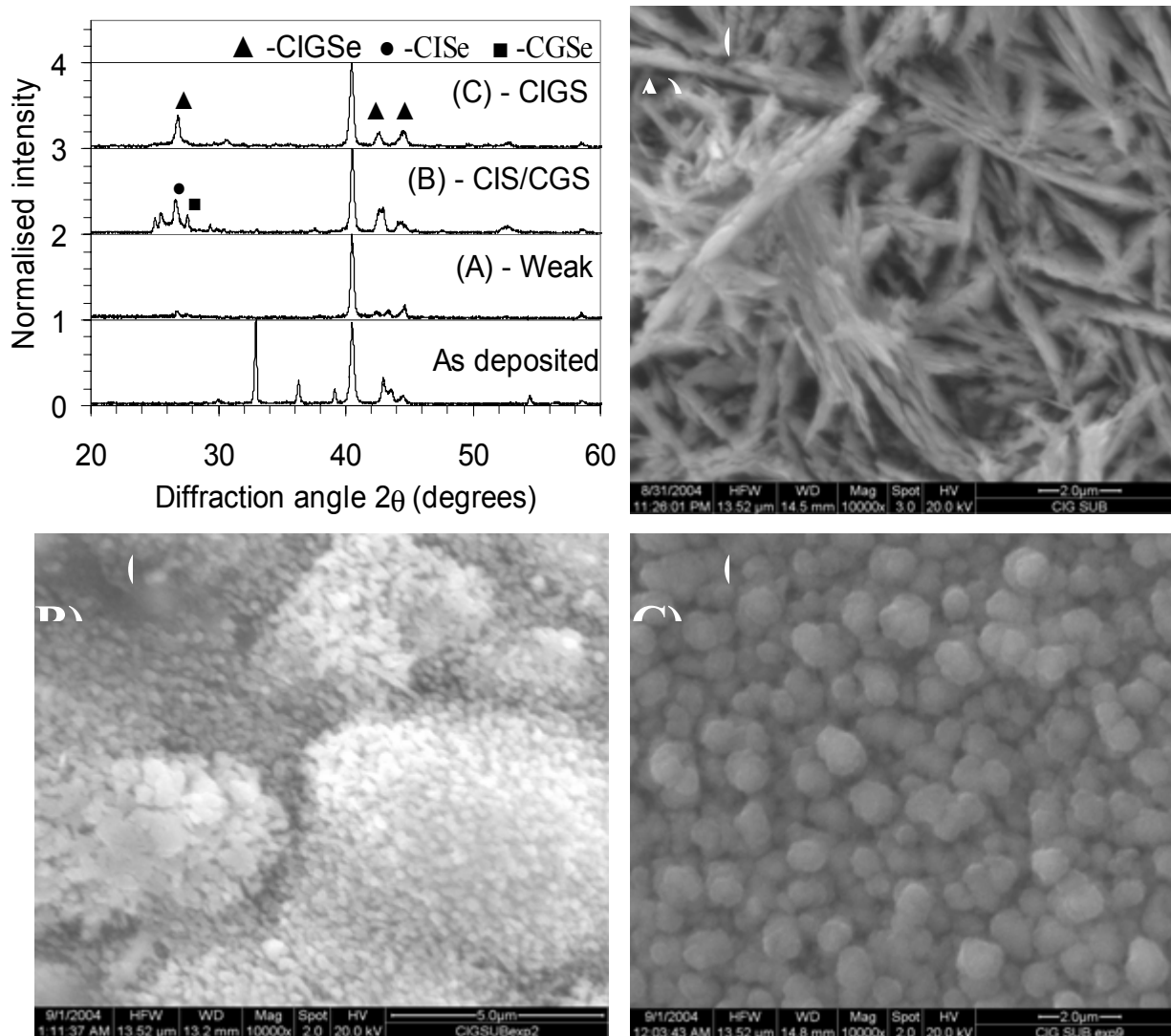
Figure 24: XRD patterns and corresponding ESEM micrographs of samples (A)-(C).

3.2   Co-evaporated Binary Compounds

Experiments examining film kinetics using the PACE chamber (Figure 2c) to co-expose a substrate to the chalcogen and one metals flux are described below.   The major findings are the following:

- The rate is controlled to first order by indium flux, and not strongly impacted by either temperature of S/In ratio.
- Plasma activation infinitely increases the reactivity of H_2S as only pure indium is formed without plasma activation, while complete β-In_2S_3 is formed with plasma activation.
- The film composition is a v*ery* strong dependence of the H_2S/In ratio. For H_2S/In ratios < 6.5 film are essentially indium, while for H_2S/In > 6.5 the films are β-In_2S_3.
- Mass spectrometer measurements indicate that at least 70% of H_2S is dissociated under typical plasma conditions.

- Film composition was largely independent of substrate temperature, however crystal orientation and quality varied significantly with temperature. We note that β-In_2S_3 was formed as low as 100ºC.

3.2.1 *Optimizing Source Operating Conditions*

Source operating conditions are considered optimized when the source can be operated with good control over time periods and rates consistent with CIGS co-evaporation, and when the chalcogen dissociation fraction is maximized.

At deposition rates similar to those typically used for CIGS co-evaporation, use of H_2S as a chalcogen source provided the tightest control of the plasma and chalcogen rate, as previously discussed on page 12. Thus, H_2S was used as the chalcogen source for examinations of co-evaporated binary compounds.

For maximum S disocciation, source power was operated at the maximum of 150 W. The limitation to 150 W is due to heating of the ICP tube. Despite using a water-cooled coil, the heat transfer away from the tube in the high vacuum PACE chamber is, of course, much less than on the benchtop. At powers above 150, the ICP tube begin to glow and eventually softens.

Determining the optimum pressure is more complex. The total amount of exited species exiting the ICP source is given by the following expression:

Total = Total Flow x Fraction Excited

With the choked flow geometry, the total flow rate exiting the ICP tube is proportional to the square root of the ICP pressure. The fraction excited is a complex function of the plasma. It is well-known that the electron temperature decreases with pressure. This is the amount of energy that the electrons have to dissociate and excite chalcogen-containing species. Because of the opposite trends in flow vs. fraction excited, we expect an optimum operating pressure. To determine this we pressure, the emission intensity at 704 nm from an excited Ar* state was measured as a surrogate of plasma intensity, since it is much more well-defined than any of the chalcogens bands or lines. The flux of excited species should then be given by:

$$Flux \propto \frac{I_{Ar*}}{\sqrt{P_{ICP}}}$$

(2)

where I_{Ar*} is the measured emission intensity

This quantity is plotted in Figure 25 using OES measurements. The flux initially increases steeply with pressure, maximizes around 150 –170 mtorr, and starts to decrease slowly. The trend indicates an optimum as expected and suggests that the optimal ICP pressure should be around ~160 mtorr.
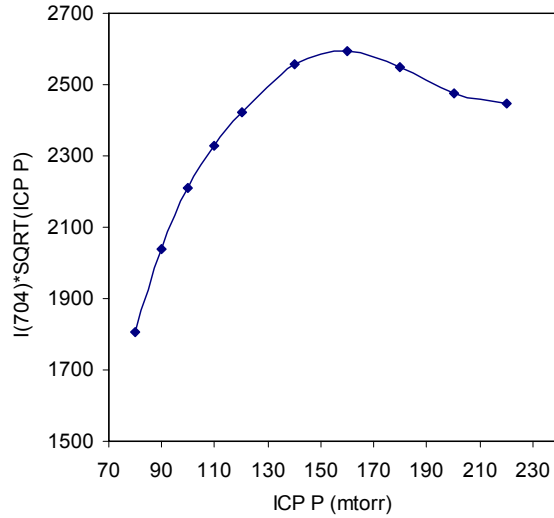
Figure 25 : Flux of excited Ar* as a function of ICP operating pressure

To test this hypothesis, a series of PACE experiments as a function of ICP pressure were performed. All experiments had in common following conditions: Indium flux: 0.3 Å/s, Gas Source: 10% H_2S in argon, ICP power = 140 W, T_s = 350 ºC. Films were deposited on 4" silicon wafers for XRD analysis and glass for optical transmission analysis. The spatial dependence of both indium flux and H_2S flux across the subject were also quantified. This arrangment allows a probing of a continuum of In: S ratios in a single deposition experiment. The qualitative results are shown in Figure 26, along with film quality distribution. The films were sectioned into 12 pieces and analyzed. For each piece there is a cluster of 3 symbols, which indicates the crystal quality as a function of 3 different operating pressures: 125, 155, and 215 mtorr. The indium evaporation boat is located directly below the edge of the sample, and its distribution follows a $1/r^2$ dependence as illustrated by the blue triangle. The ICP source has a "bulls eye" pattern, and it is directed at the center of the sample as shown in yellow.
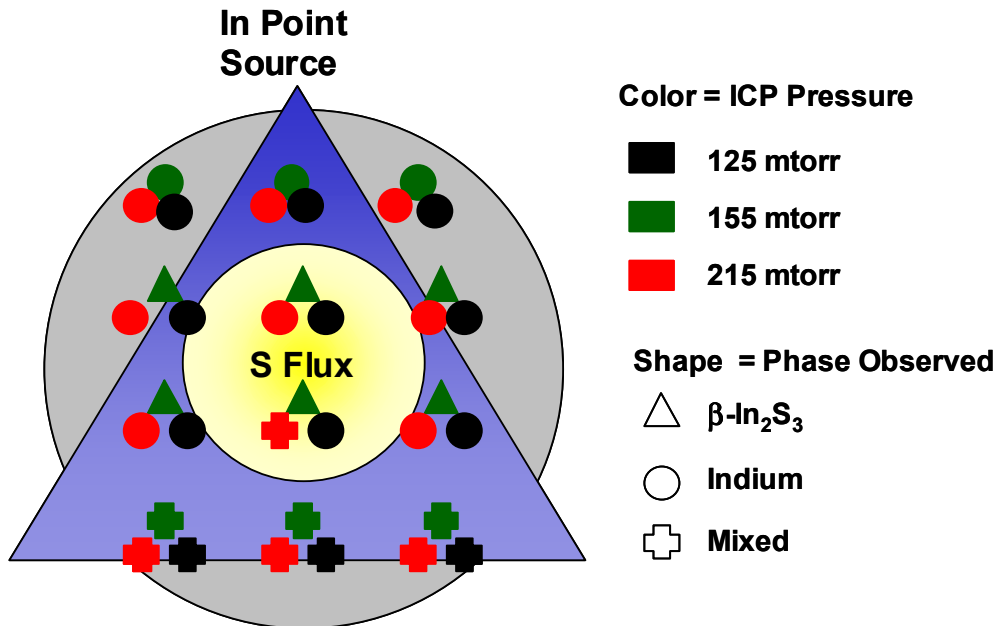
Figure 26: Schematic map of In flux(blue), S flux (yellow) across a 4" wafer, with the symbols indicating the crystal quality obtained as function of operating pressure.

23

Examples of the 3 different crystal phases are shown in Figure 27. The circles indicate that only polycrystalline indium was observed. The triangles indicate that only β-In$_2$S$_3$ was observed. The cross indicates a mixed phase, which was highly variable but usually contained both phases. In some cases peaks associated with In$_6$S$_7$ were also observed in the mixed regime. Thus Figure 27 contains a great deal of information. First, in the row of samples closest to the In source, only polycrystalline indium was observed in all experiments. Like wise in the row farthest away, a mixed phase was observed in all experiments. This is where the indium flux is the smallest. In the center two rows the results were strongly dependent on the ICP operating pressure. For the suggested optimum pressure, 155 mtorr, resulted in β-In$_2$S$_3$ formation throughout this region. In contrast, mostly polycrystalline phase was observed both at higher (215) and lower (125) pressures. The 215 mtorr experiment was slightly more effective than the 125 mtorr experiment, as some regions with mixed phase were observed. These results are in excellent agreement with the assessment of ICP performance that were shown in Figure 25.
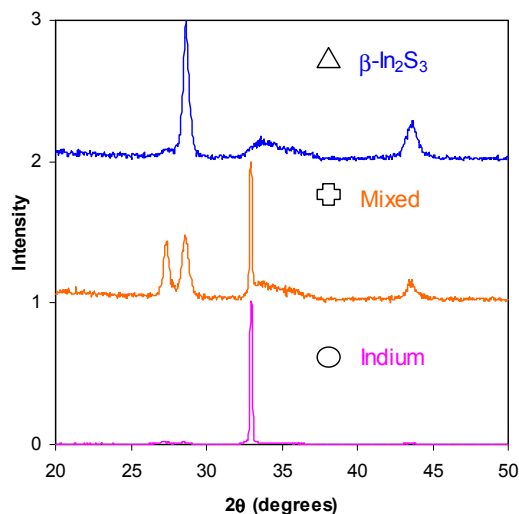
Figure 27 : Three XRD patterns exemplifying the 3 phases observed in Figure 26

Optical transmission and variable angle spectroscopic ellipsometry were also performed on samples deposited on glass and silicon, respectively. Regions with crystalline β-In$_2$S$_3$ were observed to have the appropriate band gap of ~ 2.5 eV. Likewise the refractive indices of these films were in good agreement with literature values.

A control sample was also deposited at our optimum pressure without turning on the plasma. As expected the film was essentially indium. No evidence of conversion was observed in XRD. The film had the lustrous grey color, and could be easily wiped off the substrate, and generally resembled indium films evaporated in vacuum.

3.2.2   Measuring the Dissociation Fraction

The dissociation of H$_2$S in the ICP source was quanitified. The schematic of the setup is shown in Figure 28. A residual gas analyzer (RGA) was connected to the main PACE chamber. The pressure at the RGA was further reduced using a small turbo pump to improve resolution and minimize transients in the system. It is important to note that this is not a line of site technique. The products effusing from the ICP source collide with the substrate and walls of the chamber several time before making it to the RGA. So the RGA measure what exits the ICP source plus any gas-surface reactions that follow. So we are only sensitive to stable species H$_2$S or S. Radicals such as atomic H and S recombine or condense on walls

before arriving at the RGA. The OES was used in-situ to make relative measurements of H and S using actinometry. Experiments were performed as a function of rf power and pressure, which is the ICP pressure measured upstream. In all experiments the PACE chamber itself was order 10^{-5} torr. A 10% H_2S/Ar mixture was used in all experiments. When the plasma was ignited we observed two things. Signals associated with H_2S (MW = 34) dropped and H_2 (MW = 2) increased. There was no change in the argon and no other peaks were observed.
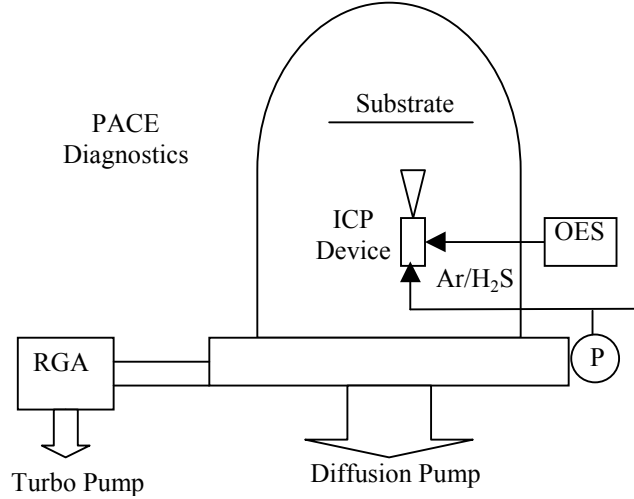
Figure 28 : Schematic of diagnostic setup

Dissociation was quantified using the following relationship

$$\%\text{Dissociation} = 100 * \frac{(H_2S_{off} - H_2S_{on})}{H_2S_{off}}$$

(3)

where off and on designate the status of the plasma. The results for power and pressure are shown in Figure 29a and b below. The results did not make sense at first. As shown in Figure 29a the H_2S dissociation starts at 60-70% for rf = 60 W, but then steadily decreases as power is increased. This is counterintuitive as one expects more dissociation at higher powers. The apparent dissociation was also slightly greater at higher pressure, which is also counter intuitive. In general pressure does not have a strong impact as shown in Figure 29b.
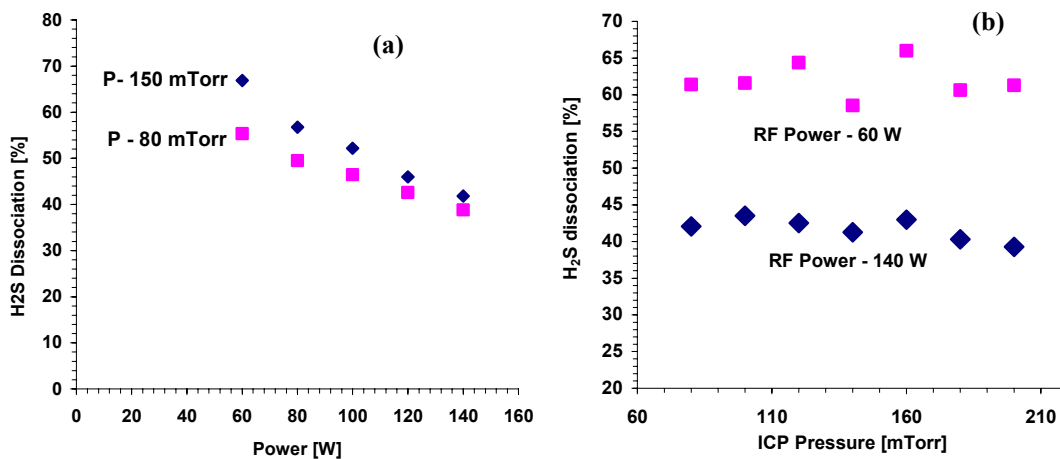
Figure 29 : %H₂S dissociation as a function of (a) power and (b) ICP pressure

The OES data clears up the picture a bit. Figure 30 plots the atomic [H] and [S] as a function of power. The atomic sulfur density remains essentially constant while the atomic hydrogen density increases linearly with power.
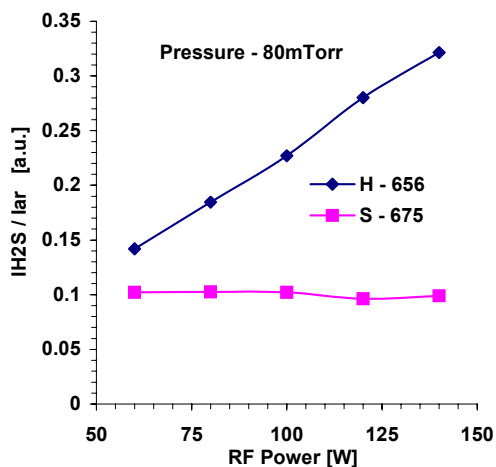
Figure 30 : . OES densities of [H] and [S] as a function of RF power.

We interpret the data in the following manner. There are two electron impact dissociation pathways:

(1) $H_2S + e- \rightarrow H_2 + S$
(2) $H_2S + e- \rightarrow 2H + S$
(3) $H_2 + e- \rightarrow 2H$

$$(4)$$

The former dominates at low power. At higher power either the second pathway becomes dominant or the hydrogen dissociation reaction becomes important. This has important consequences on the interpretation of the RGA experiments. When S exits the ICP source, we expect (and observe) it to simply condense on the cold substrate and reactor walls. If molecular hydrogen exits the ICP source, it will be unreactive and will exit the reactor. In contrast, atomic hydrogen exiting the source is very reactive and

it will react on the walls, either with itself to form H_2 or with absorbed S to remake H_2S. So in Figure 29a when we observe and apparent decrease in % dissociation with power, what we are really observing is an increase of atomic hydrogen production and related scavenging. Thus, the 70% dissociation recorded in Figure 29a may be understood to be a minimum. The true dissociation is higher, perhaps approaching 100%.

These results are interesting when compared with our deposition experience. We observe that crystallinity improves with rf power. Films at 140 W are crystalline while those at 60W contain substantial amorphous components. As shown in Figure 30, the atomic S flux is essentially unchanged under these conditions. This indicates that atomic H may play a positive role in the deposition process. This has been observed in several CVD systems. In diamond CVD atomic H improves quality by preferentially etching sp2-bonded carbon and leaving behind sp3-bonded diamond. A similar phenomenon may be occurring here. Atomic H may preferentially etch weakly bound, amorphously bonded S and leave behind crystalline β-In_2S_3. Another possibility is that atomic hydrogen recombination heats the substrate, facilitating enhanced mobility and improved film quality. We note that this may represent a significant advantage for the chalcogen hydrides over elemental chalcogens with respect to the PACE process.

3.2.3 Flux Distributions and Resulting Film Properties

The distribution of In and S inside the PACE chamber were calculated. The predicted distributions were verified by several film property measurements.

First, detailed models were developed to quantify the flux of indium and sulfur in the PACE chamber. The geometric representation of the substrate, the indium evaporation source, and ICP source are shown in Figure 31. The relative positions are given in Cartesian co-ordinates with the edge of the substrate above indium source as origin. Evaporated indium and ICP cracked gas impinge on the substrate at different fluxes depending on distance and angle from respective sources. Due to this variation of flux the indium to chalcogen ratio varies on the substrate as a function of position. By understanding this distribution the dependence of the In/S ratio can be extracted from a sinfle deposition experiment.

Physical vapor deposition from boat sources is studied extensively and the flux distribution is well established. The distribution of evaporated indium will be representative of a point source as given by equation;

$$\frac{dM_{In}}{dA} \alpha \frac{1}{r^2}$$

(5)

where M_{In} is indium flux, A is the differential area and r the relative distance from indium boat.
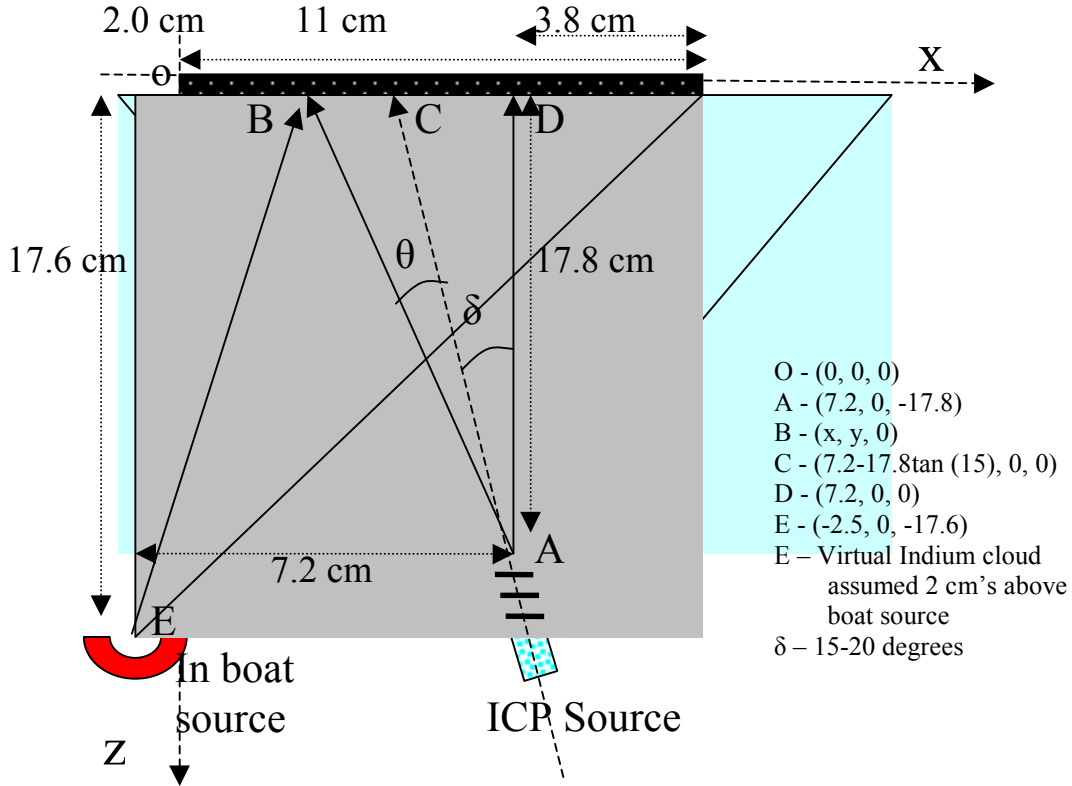
Figure 31 : Cross sectional view of substrate, Indium evaporation source and ICP source. The positions are given in Cartesian co-ordinates.

The distribution of the chalcogen source is more complicated, due to the sonic expansion as the gas exits the ICP source. The flux distribution in such sources will be representative of supersonic free jet expansion of gases in vacuum. The angular variation of density field (ρr^2) estimated from data using method of characteristics calculations is only a function of θ. The approximate relation for density variation is;

$$\rho\, r^2 \quad \alpha \quad \cos^2(\frac{\pi\theta}{2\varphi})$$

(6)

where ρ is the density of expanding gas, r - distance from jet source, θ - angle from the normal to jet source. The constant φ depends on specific heats ratio. For γ = 1.67 (argon) the value for φ is 1.365. Along a given gas stream line the speed of the gas (u) is essentially constant. The flux is give by the equation;

$$\frac{dM_{chalcogen}}{dA} = \rho u$$

(7)

Combining equations (6) and (7);

$$\frac{dM_{chalcogen}}{dA} \quad \alpha \quad \frac{\cos^2(\frac{\pi\theta}{2\varphi})}{r^2}$$

(8)

In Cartesian coordinates the distance of a given point B (x, y, 0) on substrate from ICP source A (72, 0, -178) will be;

$$r = \sqrt{(x-72)^2 + (y-0)^2 + (0-(-178))^2}$$

(9)

The angle θ is estimated using the dot product between vectors AC (axial line of ICP source) (178tan(δ), 0, 178) and AB ((x-72-178tan(δ), y, 178);

$$\theta = \cos^{-1}\left(\frac{-(x-72-178\tan(\delta))*178\tan(\delta)+0+(178)^2}{\sqrt{[178\tan(\delta)]^2+[178]^2}\sqrt{[x-72-178\tan(\delta)]^2+y^2+[178]^2}}\right)$$

(10)

Substituting (9) and (10) in (8) the chalcogen flux at point B from ICP source A can be estimated as;

$$\frac{dM_{chalcogen}}{dA} = C_2 \frac{\cos^2\left(\frac{\pi\cos^{-1}\left(\frac{-(x-72-178\tan(\delta))*178\tan(\delta)+0+(178)^2}{\sqrt{[178\tan(\delta)]^2+[178]^2}\sqrt{[x-72-178\tan(\delta)]^2+y^2+[178]^2}}\right)}{2\varphi}\right)}{(x-72)^2+y^2+(178)^2}$$

(11)

Model predictions were compared with measurements of thickness, composition and optical properties. The film discussed was deposited at T_s = 200 ºC. First it was observed that film thickness was most closely associated with the indium flux. Figure 32 compares a photograph of the sample with model predictions of the In flux variation.
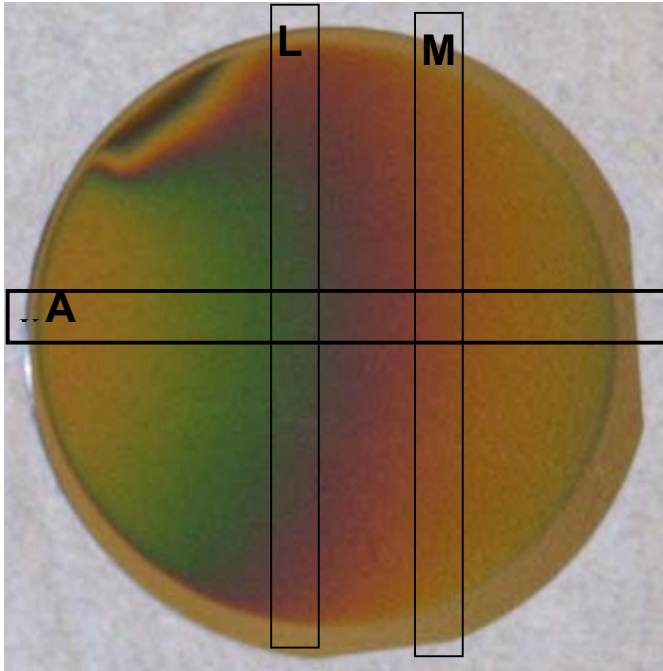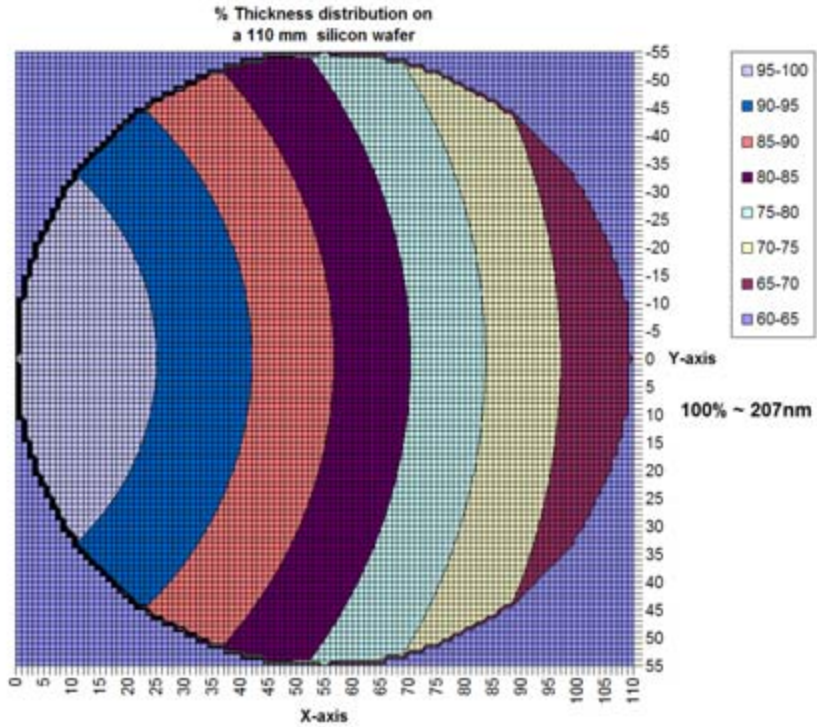
Figure 32 : Modeled In flux (top) compared with photograph of a 4" silicon sample. Note the distortion in the upper left quadrant is due to the presence of the quartz crystal microbalance.

The next figure compares the predicted sulfur distribution and the In/S ratio. The ICP source was directed to the left side of the sample as shown in the top of Figure 32. Combining this calculation with the In flux one obtains the S/In ratio. Notice the max is shifted to the right, and the gradients are steeper than in the individual elemental distributions.
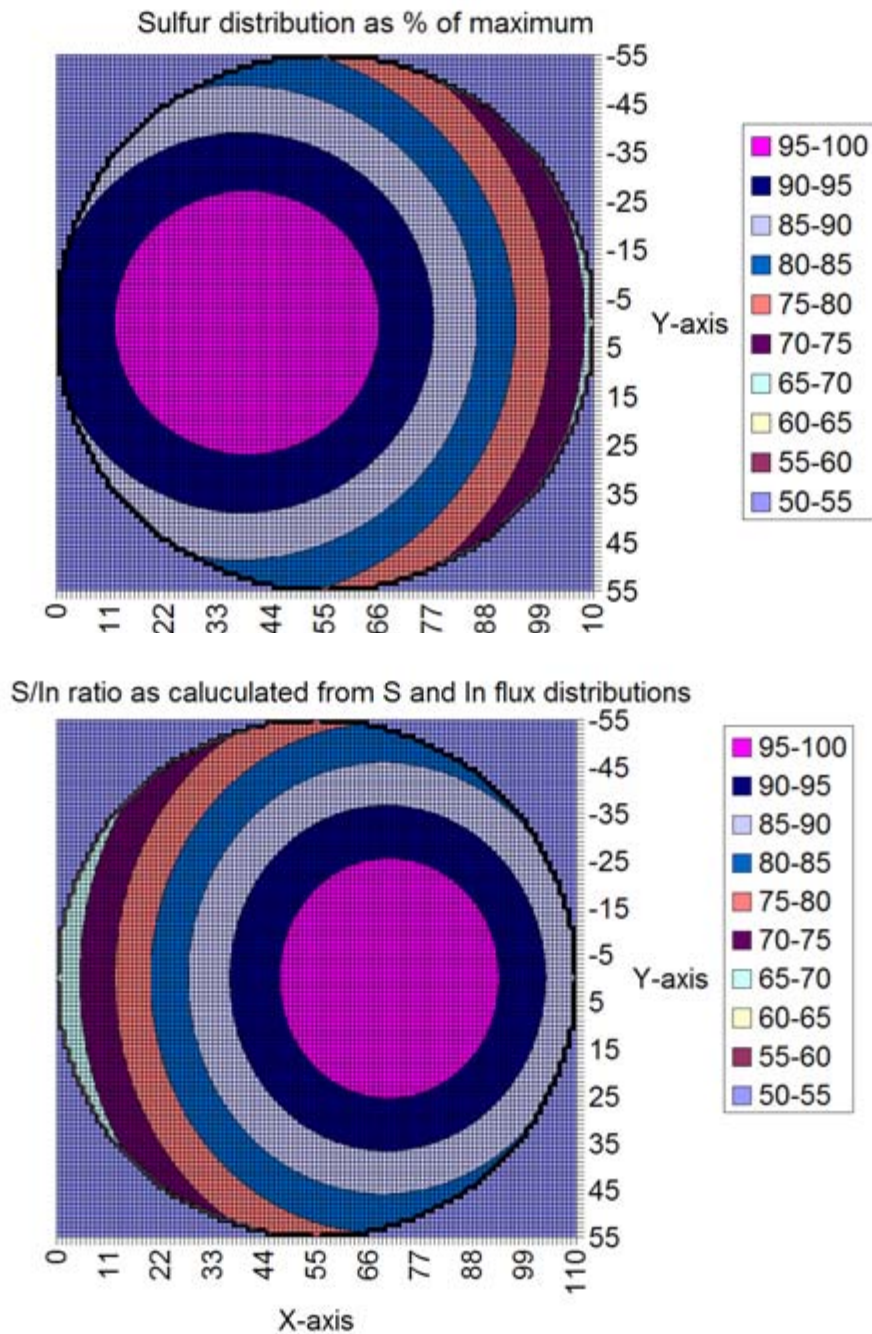
Figure 33 : Models of the sulfur distribution (top) and S/In ratio (bottom).

The thickness comparison that was shown schematically in Figure 33 was evaluated quantitatively. Figure 34 shows the measured thickness as a function of radial position across the substrate. The line is model predictions based on just the indium flux. The data contains two types of points. The red triangles were taken from the region of high sulfur flux as indicated by the purple circle in Figure 33a. The remaining data points were taken from other regions. The agreement is generally very good across the wafer. The measured thickness in the high sulfur region is slightly higher than the indium model prediction, as one would expect.

31
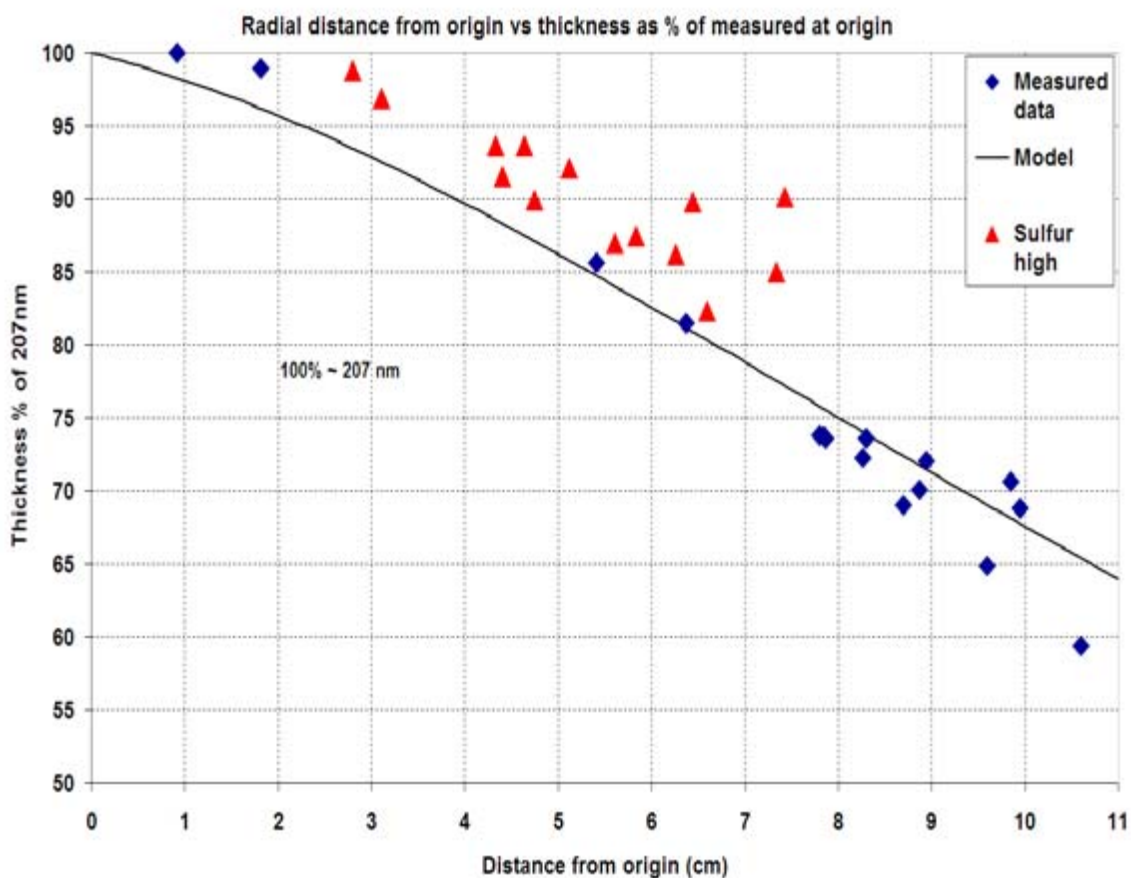
Figure 34 : Comparison of measured (points) and modeled (line) film thickness as a function of radial position from the origin.

Next we compare the properties of the as-deposited films using energy dispersive spectroscopy (EDS) for composition and spectroscopic ellipsometry (SE) for refractive index. The refractive index (n) and extinction coefficient (k) were measured across regions L and M as shown in Figure 32. The results are shown in Figure 35. As one transverses the wafer the refractive index has a sharp increase, plateaus for 2 –3 cm, and then decreases sharply. The plateau region corresponds nicely to the maxima in the S/In ratio as shown in Figure 32. We also note that the crystal structure of the films with the high refractive index display only β-In_2S_3 peaks. We also note that films outside this region displayed either In peaks or a mixture of materials.
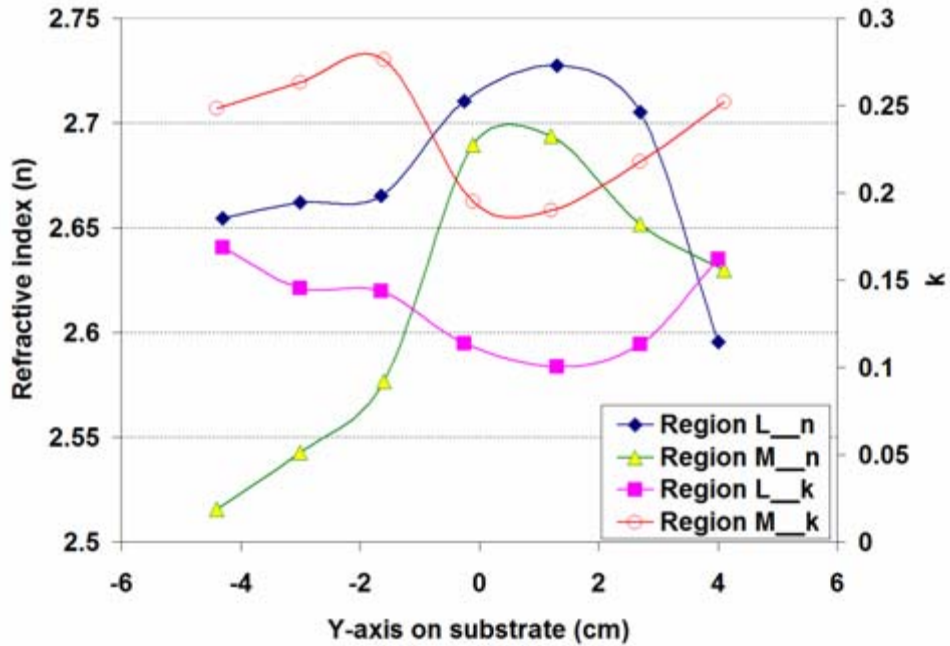
Figure 35 : Optical properties as a function of position across regions L and M as shown in Figure 32

Finally we surveyed the S/In ratio across region A using EDS. The results are shown in Figure 36. Again there is very good quantitative agreement between the data and the profiles predicted in Figure 33. The S/In ratio does not change dramatically, ~20% across the wafer, but the structural and optical properties change much more dramatically.
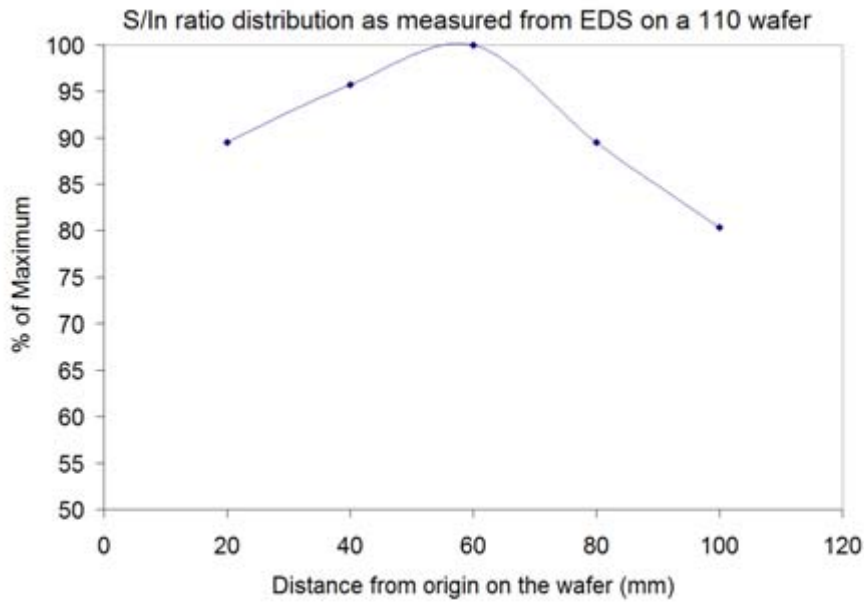
Figure 36 : S/In ratio as determined by EDS across region A.

Using the detailed models presented plus quantitative measurements of the indium deposition rates and H_2S flow rates, we established a quantitative measure of the S/In ratio. This distribution is shown in Figure 37 for a specific set of operating conditions. The data presented are all from films deposited at this condition. We also note that the ratios presented in Figure 37 represent the upper limit, assuming that all of the chalcogen is activated. In reality only a fraction of the H_2S is cracked by the ICP source. A quadrupole mass spectrometer was mounted on the on the high vacuum PACE chamber to measure this variable. The dissociation of H_2S was monitored by watching the change in the primary cracking peaks at m/z = 33 and 34. When the ICP source was turned on the H_2S signals dropped by ~ 50%, and were also accompanied by a concomitant increase in the H2 signal. Nothing else significant was observed. As discussed previously, H_2S is inactive in the PACE chamber as films deposited without plasma activation yield simply polycrystalline indium. So the ratios of active chalcogen to indium are expected to be about ½ of the values shown in Figure 37. From Figure 37 we see that the ratio can vary by approximately a factor of ~ 40% over the 4"diameter wafers.
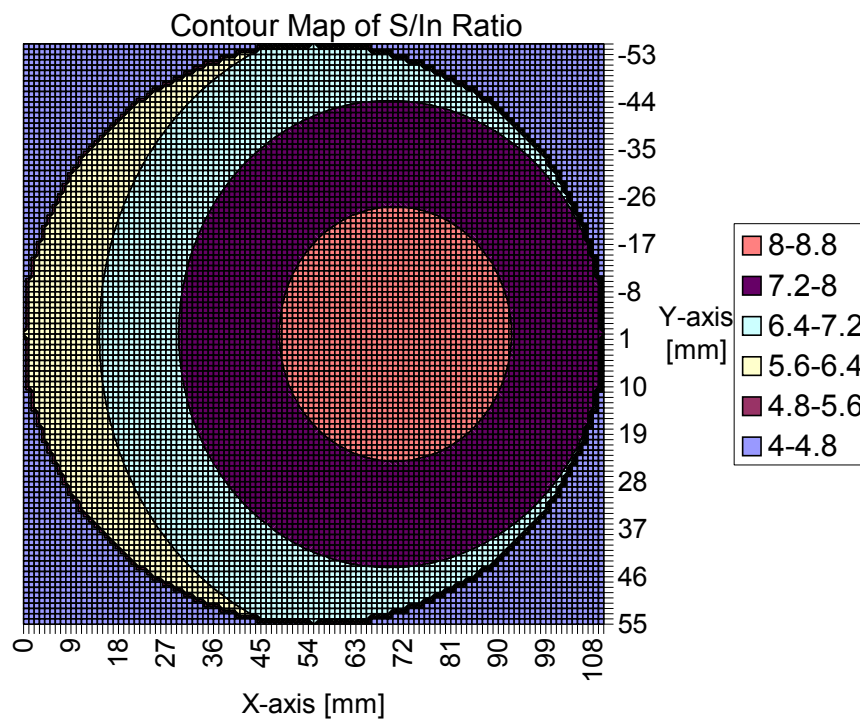
Figure 37 : Quantitative distributions of the H₂S/In flux ratios across a 4" diameter for the films described in this report.

3.2.4   Film Properties

After initial optimization of conditions for ICP operation and indium evaporation, the following conditions were used to make a sample set for further study: Indium flux: 0.3 Å/s, Gas Source: 10% H_2S in argon, ICP power = 140 W, ICP pressure = 110 mtorr, T_s = 350 ºC. Films were deposited on both silicon and glass. Figure 38 shows a photograph of a PACE film deposited on glass. The relative positions of the ICP source and indium evaporation boat are shown as well. The small sample in the picture is β-In_2S_3 that was fabricated in the benchtop system. The two samples are similar in color. The gradient in film color across the sample reflects the gradient in indium flux. The sample was sectioned into 9 pieces as shown for detailed analysis.

34
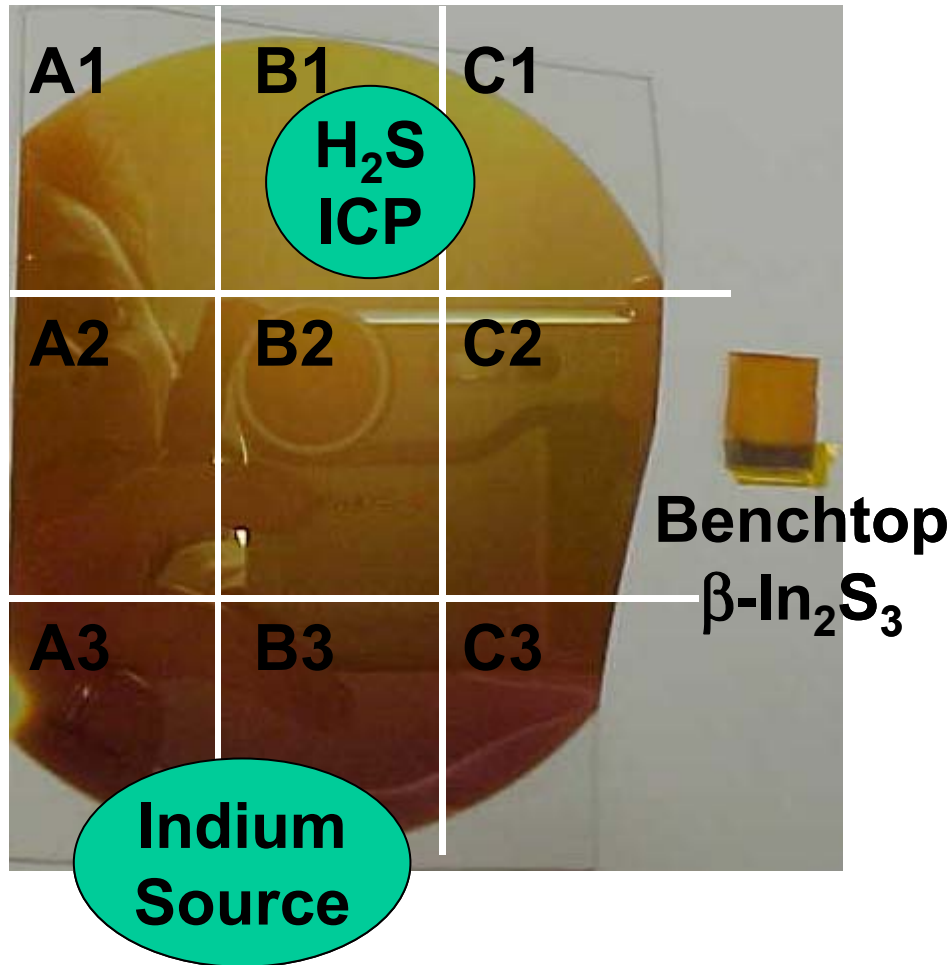
Figure 38 : Photograph of an In_xS_y film deposited by PACE, shown for comparison with a small sample of β-In_2S_3 that was produced in the bench top system. The green boxes denote the approximate positions of the indium and ICP sources. The samples were divided into 9 pieces for analysis as shown.

Figure 39 shows XRD patterns obtained from selected regions for samples deposited on glass and silicon, respectively. In both cases the crystal quality improves as the S:In ratio increases (mobbing from region 3 to region 1). In the case of glass, the patterns are dominated by the amorphous signature of the underlying glass substrate. No crystalline phases are observed at position B3, but they begin to appear in B2 and are clearly identified at B1. These two peaks are both β-In_2S_3. In the case of the silicon substrate, the XRD patterns are much more clear since there is little background. The trend is the same. In the indium-rich regions (3) there is a mixture of β-In_2S_3 and indium. As one moves to region (1) the indium peak is attenuated, and the -In_2S_3 phase becomes dominant. The sample from region C1 contained only β-In_2S_3 phases.
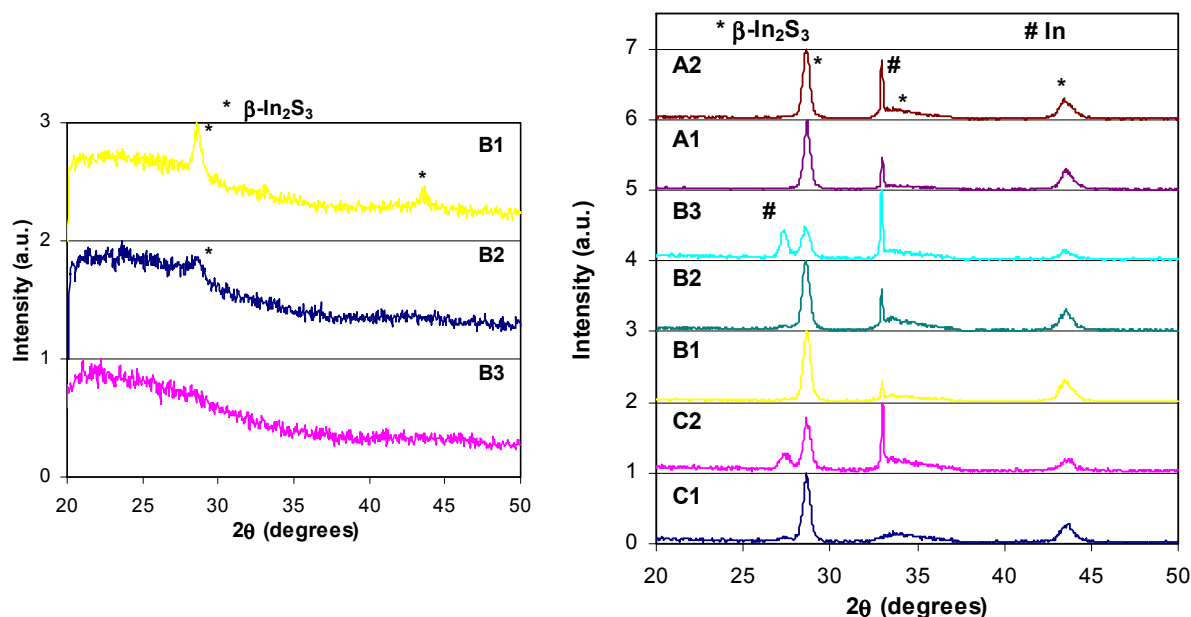
Figure 39 : XRD patterns from selected regions of co-evaporated films on glass (above) and silicon (right).

Figure 40 shows XRD patterns obtained from a single sample that was deposited at $T_s = 200$ ºC. The sample was broken into several pieces and characterized by XRD. In this figure we show XRD patterns from 2 different positions that had nominally identical S/In ratios to both validate the contour plot shown in Figure 37 and demonstrate the reproducibility of the experiment. Films deposited at S/In = 5.6 were dominated by the sharp indium peak at 33 ºC. As the ratio was increased to 6.5 strong β-In$_2$S$_3$ peaks are formed, but the In peak remains. With just a slight increase to S/In = 6.9 the indium peaks completely disappeared, and an additional β-In$_2$S$_3$ peak at 27º is observed. Films at the highest ratio of S/In = 8.3 were of course completely β-In$_2$S$_3$. The film structure is extremely sensitive to the S/In ratio, as evidenced by sharp the differences between films at 6.5 and 6.9. This was seen in other experiments as well. Two samples were grown at nominally identical conditions with the exception that the indium evaporation rate was varied 33%. The sample with the higher indium flux was almost completely indium, while the other was completely β-In$_2$S$_3$. We also note that the S/In did not have a significant impact on film thickness, which to first order is governed by the indium evaporation rate. Films in high S/In regions were 10-20 % thicker.

36
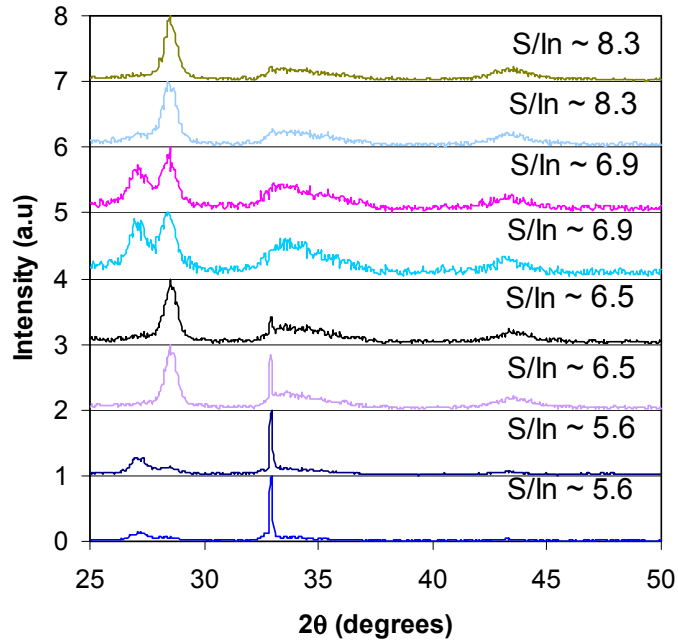
Figure 40 : XRD patterns as a function of H$_2$S/In obtained from a single sample deposited at T$_s$ = 200 ºC>

A series of films were also deposited as a function of substrate temperature. The indium and chalcogen sources were operated identically in all experiments. Figure 41 compares films deposited with a S/In ratio of ~7 as a function of temperature. In all cases the peaks displayed correspond to β-In$_2$S$_3$. Temperature was observed to have a negligible influence over the S/In ratio needed to effect the transition from indium to β-In$_2$S$_3$, however it does have an influence on crystal quality and orientation. The film orientation changes with temperature as shown in Figure 41. In addition, one observes that the peak widths and background signal both decreases with temperature, indicating higher crystal quality and a smaller amorphous component, respectively. Again, film thickness was found to be independent of temperature.
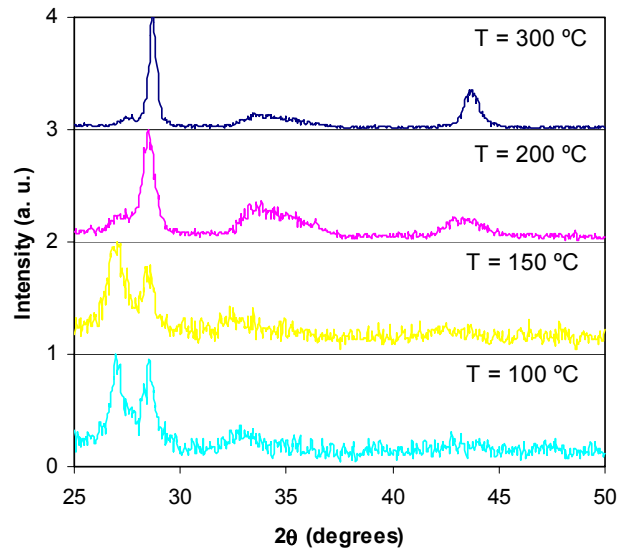
Figure 41 : XRD patterns as a function of substrate temperature for films deposited with S/In ratio of 7.

37

Figure 42 shows the AFMs at 4 substrate temperatures. As expected grain size increases with temperature, going from nanocrystalline to microcrystalline.
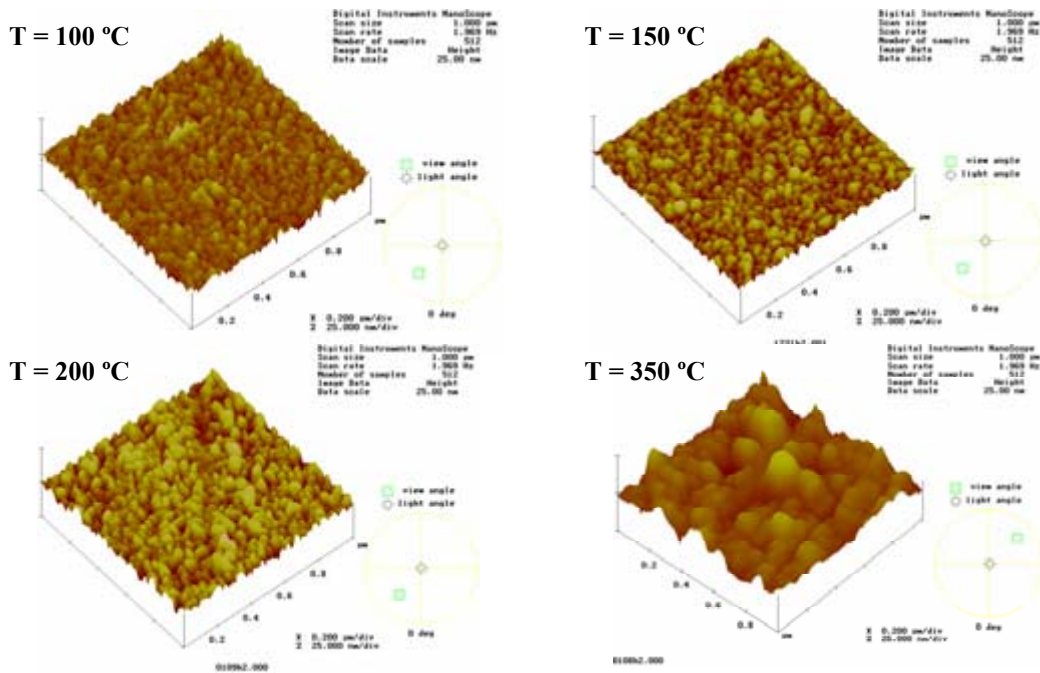
Figure 42 : AFM morphology as a function of substrate temperature.

In contrast, when depositions were performed *without* plasma activation, no S incorporation was detected by EDS or XRD. In all respects, samples fabricated without the plasma appeared to consist of metallic In.

4   Application of PACE Sources to CIGS Co-Evaporation

The PACE sources, whose development was described in previous sections, were installed in standard CIGS deposition equipment and evaluated for effect on CIGS properties.

4.1   *Baseline Process*

An important aspect of evaluating the effect of PACE sources is the demonstration of a reproducible and high quality baseline (no plasma) process for CIGS device fabrication. The bell jar used for baseline processing was described earlier (Figure 4). For baseline devices, a three-stage recipe is used to deposit CIGS onto Mo-coated glass substrates. Flux and temperature profiles from a typical deposition are shown in Figure 43. Reproducibility was improved by insuring a consistent Cu-rich excursion of the film growth, using an infrared sensor to monitor the film emissivity change as it crosses in and out of the Cu-rich regime. This method is similar to those described elsewhere using a contact thermocouple to sense the temperature change resulting from the emissivity change.[12,13] Devices were completed by application of chemical bath deposited CdS, sputtered resistive ZnO, sputtered indium tin oxide, and metallic grids. Efficiencies of completed devices are typically around 10%. Figure 44 shows an example of a CIGS device from the bell jar, with all layers deposited at ITN. The device is 1 cm^2, with no anti-reflective coating. Quoted characterization is under AM1.5, total-area conditions. Throughout the contract, a number

of adjustments to the baseline process, such as improved calibration procedures, were made to maximize reproducibility and overall efficiency.
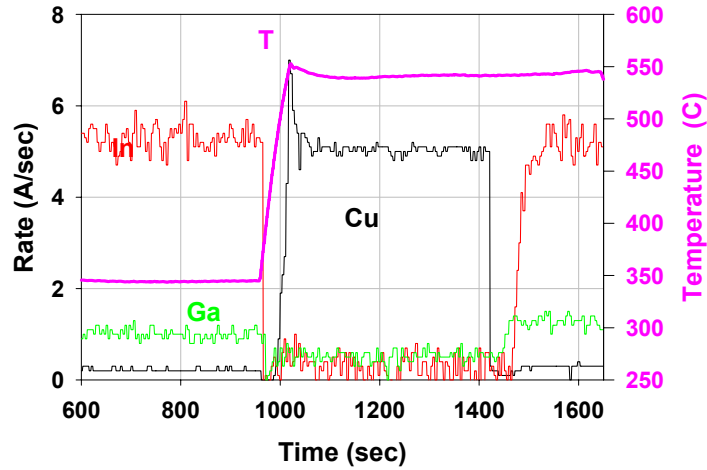
Figure 43 : Time, temperature, and deposition flux profiles for CIGS deposition.
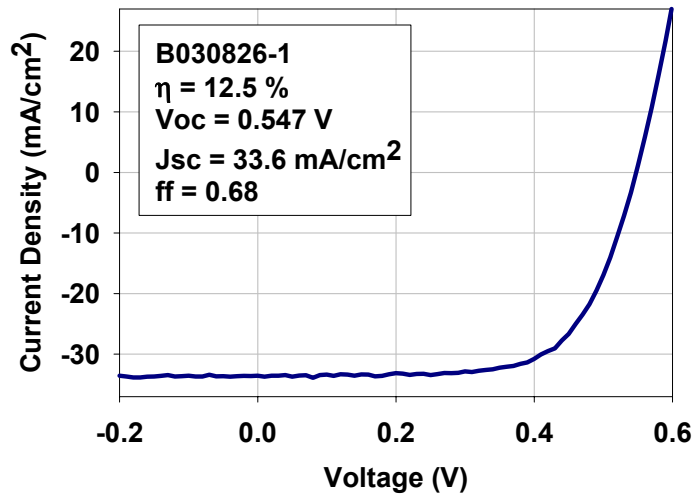
Figure 44 : JV curve of small area device from bell jar. No AR coating was applied. Cell parameters shown in inset.

4.2   Source Installation and Modification

Integration of plasma sources into full CIGS co-evaporation was performed. Incorporation of the plasma sources into three-stage CIGS co-evaporation is nontrivial, as the deposition environment exacts rigorous requirements on rate control, geometry, uniformity, resistance to heat and deposition product, and compatibility with the existing and complex sensors in the bell jar (e.g. EIES, QCM, IR).

First, necessary hardware was added to the three-stage CIGS bell jar. Use of a low-current, high-voltage Se effusion source provides flexibility in placement of the current feedthroughs relative. Effective solutions for grounding and shielding issues were implemented as demonstrated in the CSM PACE chamber. RF, Ar, and power feedthroughs were installed. To accommodate feedthroughs for RF power

and the source placement, several chamber components had to be moved, including the quartz crystal microbalance, the In source bus bar, the infrared substrate sensor, and the traditional tantalum Se boat. Argon was piped into the source area. The RF power supply and network were mounted in the chamber electrical cabinet, including the necessary 280V supply and increased cabinet cooling. Several components on the chamber that would physically obstruct the RF were relocated, including vacuum gauges, Eurotherms, and the emergency stop button. Bracketing to affix the PACE source in the chamber was fabricated and tested. A power controller for the Se pot nozzle heater was obtained and tested.

In section 2.3.4, Se from the PACE source in a test chamber was observed to follow the expected $\cos^3\theta$ flux distribution. The same flux distribution was confirmed with the PACE source installed in the three-stage bell jar. Expected flux profile was generated from the $\cos^3\theta$ flux distribution, in combination with chamber and source dimensions and orientation. This prediction is shown in Figure 45a. For experimental verification, Se from the PACE source was deposited on glass witness slides placed across the area used for substrates in CIGS depositions. As expected from earlier tests, PACE source Se rate control was acceptable in the bell jar. Multiple thickness measurements were performed across the witness slides via mechanical profilometry. The measured flux distribution is shown in Figure 45b. Two thickness measurements near some Se-coated fixturing were omitted, as some coating appears to have originated from inadvertent heating of the fixturing. There is reasonable agreement between Figure 45a and Figure 45b, considering that there are several degrees of uncertainty in the angles between the source axis and substrate. Agreement between measured and predicted PACE source flux profiles is significant because it indicates that the sources continue to function as expected, and because it provides guidelines for adjustments to sources.
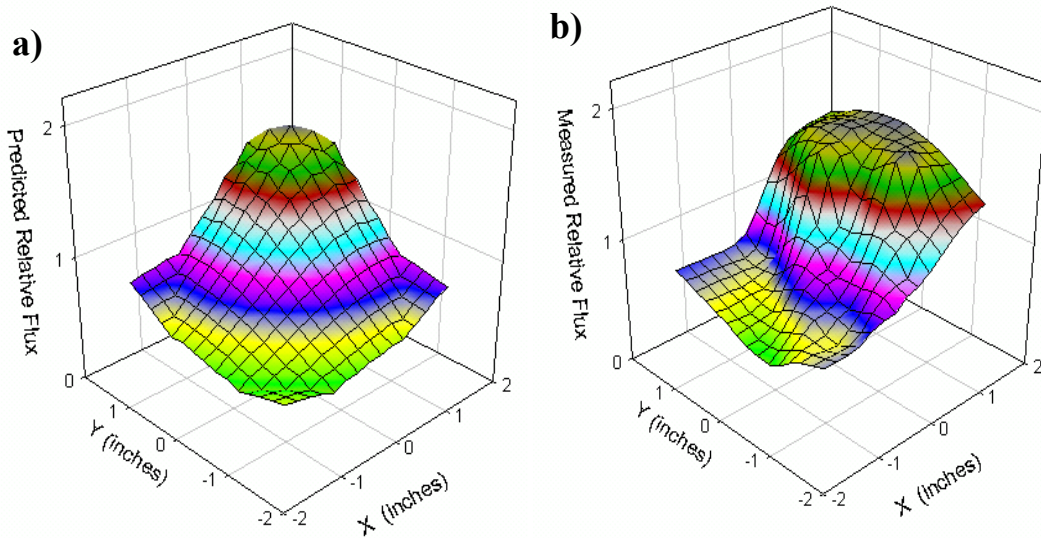
Figure 45 : a) Predicted and b) measured flux distributions from PACE source in CIGS three-stage bell jar.

Source angle was adjusted so that flux distribution is centered at the substrate center. Because the PACE source axis is not perpendicular to the substrate, and the flux falls off both with distance from the nozzle and angle off-axis, the source axis must be directed at a spot slightly beyond the substrate to center the flux distribution. The required angle for flux centering agrees well with calculations of the flux distribution.

Figure 46 shows relative flux as function of position over the substrate, during a source test. Uniformity is ± 20%, and has been demonstrated to be reproducible over several depositions. This uniformity is within limits needed to test chalcopyrite utilization in the CIGS process with and without plasma-assist. The uniformity is better than that obtained with the traditional tantalum baffled-box evaporation boat.
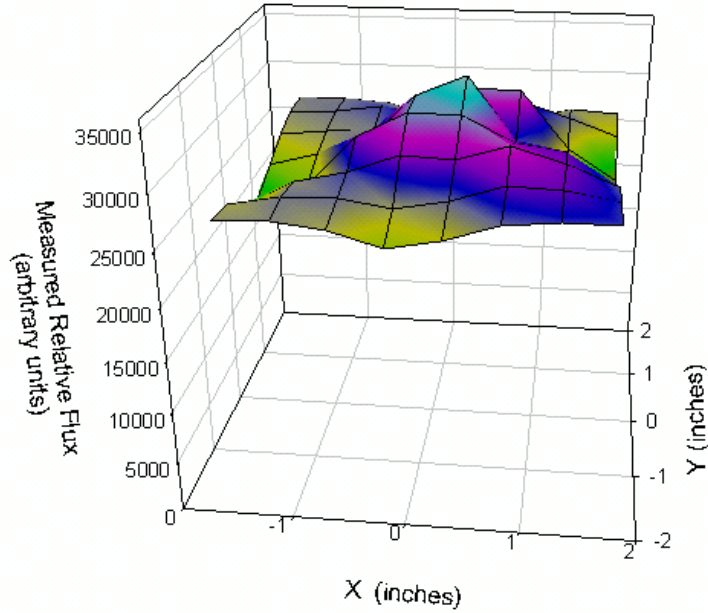
Figure 46 : Flux versus position from PACE source testing in three-stage bell jar.

The new PACE source was integrated into the fully-automated CIGS control. The automated control in the bell jar maximizes reproducibility between different depositions and operators, since all depositions are run from pre-programmed recipes. Furthermore, all measured quantities are logged to the computer for later reference. Incorporating the new PACE source into this control strategy required adding hardware and software to communicate with the PACE source temperature controllers, heat the PACE source according to computer-specified setpoints, log PACE source rates and temperatures, and allow recipe programming of these quantities. Figure 47 shows rates and temperatures from a fully-automated CIGS run incorporating a PACE source. Because the PACE source has a much larger thermal mass than the traditional Ta boat, some minor oscillations in Se rate are unavoidable. However, these ~15% oscillations are much smaller than the recommended 2 to 10x Se-to-metals ratio envelope that is considered acceptable for high-quality CIGS formation. Figure 48 shows a sample of the recipe program used to run the deposition.
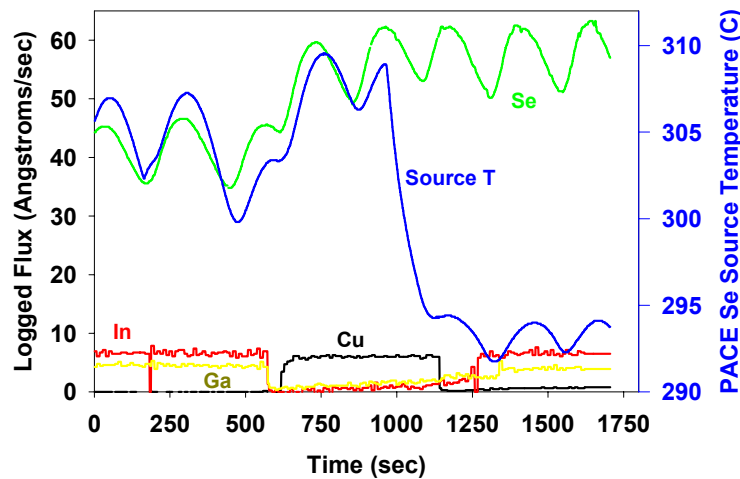
Figure 47 : Rates and temperatures from fully-automated CIGS run incorporating PACE source.

41

Figure 48 : Example portion of recipe used to program the deposition with the PACE source.

The PACE sources are not compatible with the EIES rate monitor. The data shown earlier in Figure 18 predict a 10^{-5} Torr background pressure of Ar during PACE source operation. Such pressures will add significant background noise to the already weak EIES signal. The interference is particularly severe for Ga, which is the weakest emitter of the three metals monitored by EIES. For illustration, Figure 49 shows apparent flux profiles from a CIGS deposition in which background pressure reached 8×10^{-6} Torr by the end of the second stage, due to an outgassing problem. Cu, In, and Ga rates graphed are those indicated by the EIES. Se rate is that indicated by the QCM. During the second stage (where the Cu rate is nonzero) the Ga source is turned off. However, significant rate is indicated, as circled in red, due to the increasing background pressure. The false rate is nearly equal in magnitude to the desired Ga rate, resulting, no doubt, in a significant deviation between the actual and intended Ga rates during the third stage. Ar emits efficiently at a multitude of wavelengths upon electron excitation, and is therefore exhibits a similar effect on the signal.
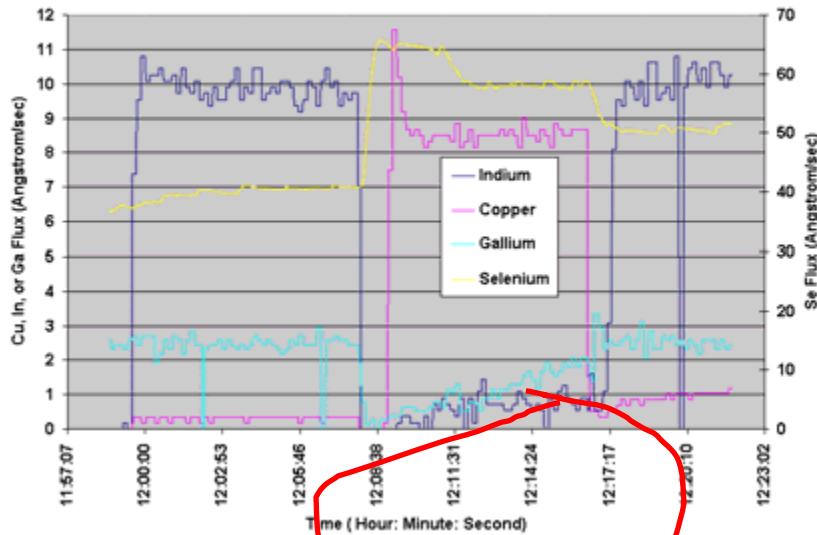
Figure 49 : Apparent flux as a function of time for three-stage CIGS deposition, with effect of background pressure increase due to outgassing circled in red.

42

Therefore, in order to avoid interference between the EIES and Ar from the PACE sources, an alternate deposition procedure was implemented. This procedure involves setting metals source rates using the EIES (without Ar flowing to the PACE source), holding the metals sources at constant deposition power while the PACE source is operating, and judging the end of the second and third stages utilizing the film emissivity. This procedure is similar to that described by Kessler et al to maintain accurate control of maximum and final Cu ratio without the use of a multi-species rate monitor. The new procedure must be flexible enough to allow for some variation in background Ar pressures due to source-to-source differences in reactor tubes. Device results on control films (without plasma) confirm that acceptable device quality is obtained using this technique.

Operation of the PACE source in the CIGS chamber is shown in Figure 47. In this photo, the PACE source is viewed by looking just under the substrate holder (black item at top of photo), and around the open substrate shutter (black item at left of photo). The bolted enclosure beneath the plasma is the Se sparger.

Figure 50 : PACE source with plasma operating in three-stage CIGS co-evaporation chamber.

As a final step in the source installation, plasma-activated Se was delivered to the substrate at rates commensurate with co-evaporation, in the three-stage CIGS co-evaporation chamber. Plasma-activated Se was delivered at a plasma power of 100 W and rate of 25 Å/sec. This rate was maintained for approximately the time of a CIGS deposition without evidence of Se condensation in the plasma tube or difficulty maintaining the plasma. Several iterations of the PACE source installation were necessary before the desired rate was obtained. It was found that

- Higher tube pressures ($\geq$500 mT Ar) and plasma powers ($\geq$60 W) are helpful in preventing coating of the quartz plasma tube with Se and preventing the plasma from vanishing into the neck of the tube.
- Chiller water temperature of 50, rather than 20, ^{o}C supplied to the RF coil also helps prevent tube coating.
- The tube should be wrapped with several layers of fiber glass to keep Ar or secondary electron generation away from the RF coil, thereby keeping the plasma confined to the inside of the reactor tube. The fiber glass also prevents coating of the RF coil with Cu, In, Ga, and Se.

- Metallic shielding should not be included, due to severe heating and subsequent shorting through the fiberglass to the RF coil.
- The IR sensor usually used for endpoint detection is responding either to RF or light from the plasma. Shielding reduced the magnitude of the noise, but not sufficiently. The resulting films were therefore off-composition. Since the system lamps and thermocouples have not been affected by the RF, in future depositions a lamp-power method of endpoint detection can be used. Endpoint detection is particularly important for these depositions, as background Ar from the plasma causes false emission in the EIES filament, thus preventing use of the EIES rate monitor when the plasma is ignited.
- After re-filling the Se sparger, Se pellets should be melted and then cooled before attempting deposition. Otherwise, spitting Se into the quartz ICP tube causes the tube to coat.
- Slight variations in the dimensions of the hand-blown quartz tubing can make a difference in how easily the plasma is ignited. A shorter neck and body on the tube is preferable.

4.3   Film Fabrication

A key anticipated benefit of PACE is the reduction of CIGS deposition temperatures. To demonstrate this advantage, CIGS was deposited at reduced temperatures known[14,15] to be detrimental to device efficiency. Some depositions were performed with plasma-activation of the chalcogen, and others without, and device performance was compared.

Operation of the PACE source during CIGS co-evaporation caused several difficulties beyond those encountered during source development. First, in order to apply the Se rates utilized during baseline CIGS processing (around 50 Å/sec), and maintain a plasma ICP pressure had to be increased to near 1 Torr. Se is more difficult to ionize than Ar, and this pressure indicates that an approximate 10:1 ratio of Ar to Se is necessary to maintain the plasma. He was also introduced into the PACE source in hopes of achieving more efficient ionization, but no benefit was realized. Second, the resulting elevated Ar pressure in the chamber (~0.5 mTorr) caused some decrease in the deposition rate and uniformity of Cu, In, and Ga fluxes. This Ar-dependent rate increase is particularly problematic since the EIES rate sensor cannot be used during PACE source operation, and depositions with plasma therefore rely on a calibrated constant source power (as described on page 43). Third, the IR sensor used for endpoint detection responds significantly to light from the ICP tube. Thus, the operator's only indications of film emissivity during a PACE deposition are changes in lamp power required to maintain a given substrate temperature. Such changes are often difficult to distinguish from thermal transients related to chamber and source heating. Finally, although coating of the RF coil was mitigated by wrapping it in fiberglass, the coil's occasional degradation required re-building the source with a fresh Cu coil when plasma ignition failed.

These operational difficulties caused composition control to be difficult for the PACE films. Composition control is important both for creating acceptable final film properties, and insuring that the film experiences the Cu-rich growth period that has been demonstrated to have an important effect on CIGS films grown at low temperatures. Many PACE depositions failed because the final film composition was not within the desired Cu/(In+Ga) atomic ratio envelope of 0.8 to 0.95.

Difficulties in controlling composition when operating the PACE source prompted the use of three different CIGS recipes: three-stage,[16] two-stage,[17] and "Cu-first". The standard three-stage CIGS recipe requires endpoint detection for the second stage, when the film is mildly Cu-rich, and for the third stage, when the film returns to Cu-poor. A two-stage recipe, in which Cu and In are deposited simultaneously during the initial portion of the deposition, requires only one instance of endpoint detection, and therefore may allow better composition control under difficult circumstances. However, if the high Ar pressure causes significant decrease in Cu rate from that intended, even the two-stage film may not experience Cu-rich growth. To avoid this lack of Cu-rich growth, a modified two-stage deposition was also performed where all Cu was deposited before the In. This recipe is referred to in this report as "Cu-first".

CIGS films were formed into devices using the standard baseline window layers described in section 4.1.

4.4   Device Analysis

PACE and control (no plasma) films were deposited as a function of maximum substrate temperature and CIGS recipe. Table 2 shows a summary of these deposition conditions, film composition, and the resulting device performance. The same information is presented graphically in Figure 51. In Figure 51, hollow points show devices made without plasma activation, and solid points show those made with the plasma. Circles show films made using the three-stage recipe, while squares denote the two-stage recipe, and triangles the Cu-first recipe. No benefit is detected from the addition of plasma activation. In fact, in its current implementation, equipment difficulties are a significant deterrent.

Device	Efficiency (%)	Voc (V)	Jsc (mA/cm2)	Fill Factor	Total Thick-ness (Ang.)	Cu/ (In+Ga)	Ga/ (In+Ga)	Recipe	Max T (C)	Plas-ma?
B040113-1-8	9.78	0.569	30.57	0.56	27819	0.872	0.352	3 stage	575	N
B040525-2-A1	9.71	0.519	28.17	0.66	22292	0.765	0.382	3 stage	575	N
B040526-1-D5	9.36	0.504	28.82	0.64	21009	0.723	0.402	3 stage	575	N
B040603-1-D5	9.16	0.522	26.87	0.65	21911	0.79	0.366	3 stage	400	N
B040929-3-B2	8.78	0.527	29.17	0.57	27156	0.835	0.371	2 stage	565	N
B040930-1-E6	9.15	0.478	32.09	0.6	26406	0.901	0.135	2 stage	500	N
B040930-2-B5	7.55	0.486	25.74	0.6	25850.3	0.813	0.147	2 stage	565	N
B041203-2-A1	6.69	0.486	27.33	0.5	14363	0.83	0.258	2 stage	400	Y
B041214-1-E1	7.92	0.479	30.08	0.55	18554	0.985	0.22	2 stage	400	Y
B050124-1-A1	2.09	0.239	23.77	0.37	14047	0.978	0.189	2 stage	400	Y
B050207-2-E1	5.02	0.369	27.23	0.5	18563	0.926	0.251	Cu first	400	Y
B050224-1-E6	7.83	0.497	23.63	0.67	24938	0.802	0.232	Cu first	400	Y

Table 2: Summary of CIGS deposition conditions, composition, and device performance.
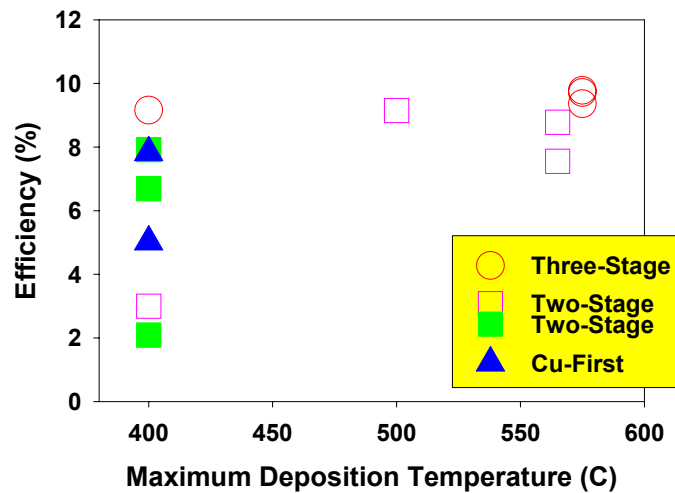

Figure 51: Device performance as a function of maximum deposition temperature, recipe, and plasma-activation (solid points).

4.5   Discussion

The lack of benefit from plasma activation is in sharp contrast with the benefits evident from benchtop source experiments (section 3.1). The direct incorporation of PACE sources into CIGS co-evaporation, with high Se rates is problematic for several reasons:
- It is difficult to establish low-pressure discharges using only elemental chalcogen, and significant amounts of argon must be added to stabilize the plasma.
- The extra argon increases the ICP pressure, which decreases the electron temperature, exponentially decreasing the ability of electrons to dissociate chalcogen.
- The argon increases the deposition chamber pressure, detrimentally impacting metal evaporation sources and impacting other equipment in the process.
- Elemental chalcogens will condense in the ICP source below T< 250 ºC. This is especially problematic during ICP ignition and extinction. This requires extraordinary operational care and perhaps external heating to prevent this from occurring.

It is possible that these disadvantages might be overcome if one were to modify the CIGS co-evaporation process to use $H_2(S,Se)$ instead of elemental Se, analogous to the work for formation of In_2Se_3 (section 3.2). The use of gaseous precursors (H_2S/ H_2Se) offers several benefits over the elemental chalcogen. First, H plasmas are easy to sustain in the ICP source, so the use of gaseous precursors can eliminate the need for argon. Second, a significant amount of atomic H is made in the ICP source, which recombines to H_2 on the walls. This is an exothermic reaction which heats the ICP source to temperatures >200 ºC. This *in-situ* heating prevents chalcogen condensation and keeps the ICP source clean while allowing the ICP coil to remain fully water-cooled. Third, atomic H exiting the ICP source will also recombine on at the substrate. The associated heating may be beneficial for film growth. This has been seen in other CVD systems such as diamond deposition. In the PACE chamber it has been observed that increasing the RF power increases the atomic hydrogen density, but the atomic sulfur density remains unchanged. Film properties improve with rf power, suggesting that H is indeed beneficial to film growth. Finally, gaseous precursors are expected to supply more energy to the growing film, since elemental chalcogens sublime as long chain oligomers and likely require multiple electron collisions to be fully reduced to chalcogen atoms. It is clear from the emission spectroscopy data that the ICP source produces significant quantities of diatomic chalcogens (S_2, Se_2). However, the diatomic chalcogens do not supply a significant amount of energy. As shown in Figure 52, the difference between S_8 and S_2 is only about 8 kcal/atm. In contrast, the benefit in going from S_2 to S is about 50 kcal/atom. The energy difference between diatomic chalcogen and gaseous chalcogen is not substantial. Elemental vapors will require multiple electron impact reactions to decompose the oligomers, while a single collision is required for gaseous sources.

$$H_2S + e^- \rightarrow H_2 + S + e^-$$
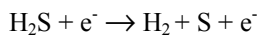
This decomposition has been observed experimentally. Emission spectra using elemental vapors are dominated by diatomic chalcogen bands, and the signal from atomic species in very weak and often cannot be resolved from the background. In contrast, large atomic emission peaks are clearly seen in the H_2S plasmas, and the band emission from the diatomic chalcogens is significantly attenuated. PACE chamber experiments demonstrated that H_2S is nearly complete, with > 70% dissociation (section 3.2.2). Since H_2Se is less stable than H_2S, it is expected that complete dissociation of H_2Se would also be achieved in a plasma.
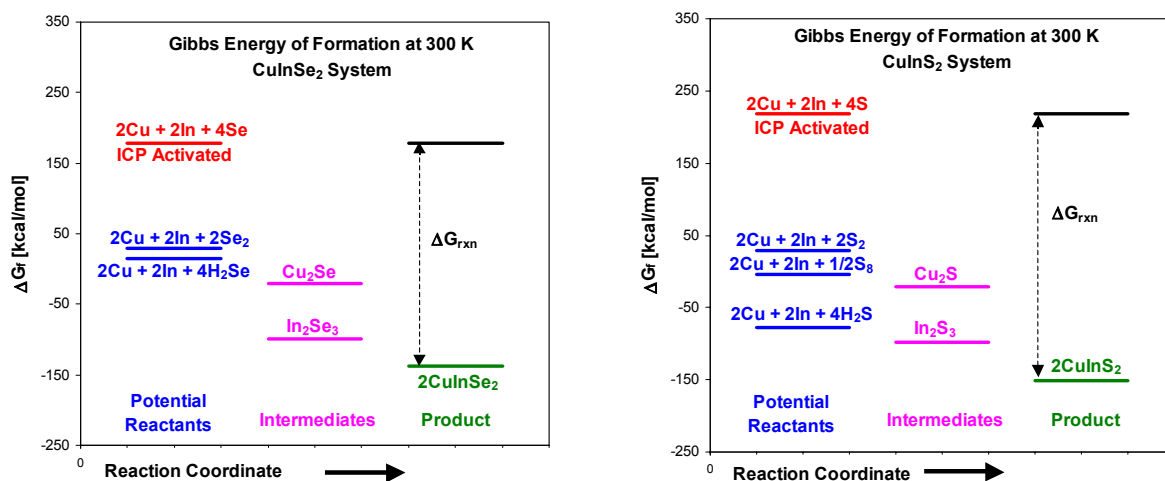
Figure 52:Potential Energy diagram for copper chalcopyrite formation from different sources.

5   Team Activities

ITN and CSM participate in team activities.   This participation has included facilitation of absorber sub-team activities, analysis and discussion of team data in absorber sub-team transport studies, admittance spectroscopy measurements on the same samples, attendance and presentations at team meetings, assembly of a publication describing absorber sub-team activities, and work with NREL scientists to sulfurize high-efficiency CIGS material.

6   Conclusions and Future Directions

This program explored the use of plasma-activated chalcogen sources in CIGS co-evaporation to lower CIGS deposition temperature, increase utilization, increase deposition rate, and improve S:Se stoichiometry control.

Plasma activation sources were designed and built, then operated and characterized over a wide range of conditions. Optical emission and mass spectrometry data show that chalcogens are effectively dissociated in the plasma.

The enhanced reactivity achieved by the plasma processing was demonstrated by conversion of pre-deposited metal films to respective chalcogen-containing phases at low temperature and low chalcogen flux. Three material systems (In, Cu-In, Cu-In-Ga) were successfully converted to sulfides and selenides using plasma processing. Films treated at the highest temperature thermally showed no or little chalcogen conversion. The binary b-In_2S_3 phase was formed at 250 ºC, while ternary and quaternary phases were formed by plasma processing at 350 ºC in less than one hour. Films with well-defined XRD patterns were also characterized by proper optical band gaps and a well-defined polycrystalline morphology.

The PACE sources were also implemented in CIGS co-evaporation. No benefit from PACE was observed in device results and frequent deposition failures occurred. Use of the PACE sources with

elemental Se and the high rates typical of co-evaporation pose a number of equipment and physical problems. It is difficult to establish low-pressure discharges using only elemental chalcogen, and significant amounts of argon must be added to stabilize the plasma. High rates require high Ar pressures, causing interference with composition control and decreasing the ability of electrons to dissociate chalcogen. Avoiding condensation of the chalcogen in the ICP source requires extraordinary operational care and results in frequent deposition failures.

It is possible that these disadvantages might be overcome if one were to modify the CIGS co-evaporation process to use $H_2(S,Se)$ instead of elemental Se, analogous to the work performed to form In_2S_3 (section 3.2). H plasmas are easy to sustain in the ICP source, so the use of gaseous precursors can eliminate the need for argon. A significant amount of atomic H is made in the ICP source, which recombines to H_2 on the walls, preventing condensation. Finally, gaseous precursors are expected to supply much more energy to the growing film.

It is thus reasonable that future studies in this area would attempt CIGS formation through use of gaseous precursors. Two unknowns are involved in this alternate approach. First, while >19% devices have been produced using elemental Se, the process space for utilizing gaseous precursor during co-evaporation is largely unknown. Second, significant safety issues must be addressed for use of H_2Se.

7   Publications

1.   S. Kosuarju, I. Repins, C. A. Wolden, "Development of Plasma-assisted Processing for Selenization and Sulfurization of Absorber Layers", *Proceedings of the 2003 National Center for Photovoltaics Review Meeting*, 2003.

2.   S. Kosaraju, C.A. Wolden, I. Repins, "Development of Plasma-assisted Processing for Selenization and Sulfurization of Absorber Layers", Materials Research Society Symposium **763**, pp. 391-396, 2003.

3.   S. Kosaraju, I.L. Repins, C.A. Wolden, "Formation of Chalcogen Plasmas and their Use in Synthesis of Photovoltaic Absorbers," *DOE Solar Energy Technologies Program Review Meeting: Government Document #DOE/GO-102005-2067*, (2004).

4.   S. Kosaraju, I.L. Repins, C. A. Wolden, "Formation of chalcogen containing plasmas and their use in the synthesis of photovoltaic absorbers," *Journal of Vacuum Science and Technology*, in press, 2005.

5.   I.L. Repins, B.J. Stanbery, D. L. Young, S.S. Li, W. K. Metzger, C.L. Perkins, W.N. Shafarman, M. E. Beck, L. Chen, V. K. Kapur, D. Tarrant, M.D. Gonzalez, D.G. Jensen, T.J. Anderson, X. Wang, L.L. Kerr, B. Keyes, S. Asher, A. Delahoy, B. Von Roedern, "Comparison of Device Performance and Measured Transport Parameters in Widely-Varying Cu(In,Ga)(Se,S) Solar Cells," *Progress in Photovoltaics*, in press, (2005).

8   References

[1] 78th Edition of the CRC Handbook of Chemistry and Physics, 78th Ed, Editor D. R. Lide, (CRC Press, Boca Raton) 1997.

[2] H. Migge and J. Grzanna, "Thermochemistry in the system Cu-In-S at 723K," *J. Mater. Chem.*, **9** (1994.) pp. 125-128.

[3] M. V. Malyshev and V.M. Donnelly, "Diagnostics of chlorine inductively coupled plasmas. Measurement of electron temperatures and electron energy distribution functions," *J. Appl. Phys.,* **87** (2000) pp. 1642-1648.

[4] E. Meeks, R.S. Larson, P. Ho, C. Apblett, S. M. Han, E. Edelberg, and E. S. Aydil, "Modeling of SiO_2 deposition in high density plasma reactors and comparisons of model predictions with experimental measurement," *J. Vac. Sci. Technol. A*, **16** (1998) pp. 544-563.

[5] I.L. Repins, D. Fisher, W.K. Batchelor, L. Woods, M.E. Beck, "A Non-Contact Low-Cost Sensor for Improved Repeatability in Co-Evaporation of High-Quality CIGS", *Progress in Photovoltaics*, in press, 2005.

[6] R.W. Birkmire, W.N. Shafarman, E. Eser, S.S. Hegedus, B.E. McCandless, R. Aparicio, K. Dobson, "Optimization of Processing and Modeling Issues for Thin Film Solar Cell Devices Including Concepts for the Development of Polycrystalline Multijunctions", *Annual Report to NREL under Subcontract ZAK-8-17619-33*, 2001, pp. 3-4.

[7] C. A. Wolden, S. Mitra, and K. K. Gleason, J. Appl. Phys. **72**, 3750 (1992).

[8] J. I. Pankove, *Optical Processes in Semiconductors*. (Prentice Hall, Englewood, NJ, 1972) p. 248.

[9] N. Barreau, S. Marsillac, J. C. Berne`de, T. B. Nasrallah, and S. Belgacem, Phys. Stat. Sol. **184**, 179 (2001).

[10] T. Walter and H. W. Schock, Thin Solid Films **224**, 74 (1993).

[11] M. Murudachalam, R. W. Birkmire, H. Hichri, J. M. Schultz, A. Swartzlander, and M. M. Al-Jassim, J. Appl. Phys. **82** (1997).

[12] J. Kessler, J. Scholdstrom, L. Stolt, "Rapid $Cu(In,Ga)Se_2$ Growth Using "End Point Detection", *Proceedings of the 28th IEEE Photovoltaics Specialists Conference*, (2000), pp. 509-512.

[13] K. Ramanathan, M.A. Contreras, C.L. Perkins, S. Asher, F. S. Hasoon, J. Keane, D. Young, M. Romero, W. Metzger, R. Noufi, J. Ward, A. Duda, "Properties of 19.2% Efficiency $CuInGaSe_2$ Thin-film Solar Cells", *Progress in Photovoltaics: Research and Applications*, Vol. **11**, (2003), pp. 225-230.

[14] M. Lammer, U. Klemm, M. Powalla, "Sodium co-evaporation for low temperature Cu(In,Ga)Se2 deposition," *Thin Solid Films* **387**, (2001), pp. 33-36.

[15] W.N. Shafarman, J. Zhu, "Effect of Grain Size, Morphology, and Deposition Temperature on $Cu(InGa)Se_2$ Solar Cells," *Materials Research Society Symposium Proceedings* **668**, (2001), pp. H2.3.1-H2.3.6.

[16] A.M. Gabor, J.R. Tuttle, D.S. Albin, M.A. Contreras, R. Noufi, A.M. Herman, "High-efficiency $CuIn_xGa_{1-x}Se_2$ solar cells made from $(In_x,Ga_{1-x})_2Se_3$ precursor films", *Applied Physics Letters*, **65**(2), pp. 198-200, (1994).

[17] Hedstrom, H. Ohlsen, M. Bodegard, A. Kylner, L. Stolt, D. Hariskos, M. Ruckh, H.W. Schock, *Proceedings of the 23rd IEEE Photovoltaics Specialists Conference*, 364-371 (1993).

REPORT DOCUMENTATION PAGE

Form Approved
OMB No. 0704-0188

1. REPORT DATE *(DD-MM-YYYY)*	2. REPORT TYPE	3. DATES COVERED *(From - To)*
August 2005	Subcontract Report	December 2001 – April 2005

4. TITLE AND SUBTITLE
Plasma-Assisted Co-evaporation of S and Se for Wide Band Gap Chalcopyrite Photovoltaics: Final Subcontract Report, December 2001 – April 2005

5a. CONTRACT NUMBER
DE-AC36-99-GO10337

5b. GRANT NUMBER

5c. PROGRAM ELEMENT NUMBER

6. AUTHOR(S)
I. Repins and C. Wolden

5d. PROJECT NUMBER
NREL/SR-520-38357

5e. TASK NUMBER
PVB55101

5f. WORK UNIT NUMBER

7. PERFORMING ORGANIZATION NAME(S) AND ADDRESS(ES)
ITN Energy Systems, 8130 Shaffer Parkway, Littleton, Colorado 80127
Colorado School of Mines, Golden, Colorado 80401

8. PERFORMING ORGANIZATION REPORT NUMBER
NDJ-2-30630-11

9. SPONSORING/MONITORING AGENCY NAME(S) AND ADDRESS(ES)
National Renewable Energy Laboratory
1617 Cole Blvd.
Golden, CO 80401-3393

10. SPONSOR/MONITOR'S ACRONYM(S)
NREL

11. SPONSORING/MONITORING AGENCY REPORT NUMBER
NREL/SR-520-38357

12. DISTRIBUTION AVAILABILITY STATEMENT
National Technical Information Service
U.S. Department of Commerce
5285 Port Royal Road
Springfield, VA 22161

13. SUPPLEMENTARY NOTES
NREL Technical Monitor: H. Ullal

14. ABSTRACT *(Maximum 200 Words)*
In this work, ITN Energy Systems (ITN) and lower-tier subcontractor Colorado School of Mines (CSM) explore the replacement of the molecular chalcogen precursors during deposition (e.g., Se_2 or H_2Se) with more reactive chalcogen monomers or radicals (e.g., Se). Molecular species are converted to atomic species in a low-pressure inductively coupled plasma (ICP). This program explored the use of plasma-activated chalcogen sources in CIGS co-evaporation to lower CIGS deposition temperature, increase utilization, increase deposition rate, and improve S:Se stoichiometry control. Plasma activation sources were designed and built, then operated and characterized over a wide range of conditions. Optical emission and mass spectrometry data show that chalcogens are effectively dissociated in the plasma. The enhanced reactivity achieved by the plasma processing was demonstrated by conversion of pre-deposited metal films to respective chalcogen-containing phases at low temperature and low chalcogen flux. The plasma-assisted co-evaporation (PACE) sources were also implemented in CIGS co-evaporation. No benefit from PACE was observed in device results, and frequent deposition failures occurred.

15. SUBJECT TERMS
PV; manufacturing; module; molecular chalcogen precursors; inductively coupled plasma (ICP); wide band gap; mass spectrometry; plasma assisted co-evaporation (PACE);

16. SECURITY CLASSIFICATION OF:			17. LIMITATION OF ABSTRACT	18. NUMBER OF PAGES	19a. NAME OF RESPONSIBLE PERSON
a. REPORT	b. ABSTRACT	c. THIS PAGE	UL		
Unclassified	Unclassified	Unclassified			**19b. TELEPONE NUMBER** *(Include area code)*

Standard Form 298 (Rev. 8/98)
Prescribed by ANSI Std. Z39.18

F1146-E(05/2004)